

Dear researcher,

The following pages fix the errors that have been overlooked during the final production stage of the book. They also introduce language modifications for better clarity. Please make appropriate changes to your copy.

We continuously try to keep this document up-to-date and, thus, appreciate if you could bring to our attention errors or unclear statements that are already not included in this file. Please email your corrections/suggestions to [yazdani@ryerson.ca](mailto:yazdani@ryerson.ca)

Thanks

A. Yazdani  
R. Iravani

Last updated Aug. 2, 2016

**On Dec. 19, 2012, the following changes were made to the Dec. 17, 2012 version of this document:** Errors fixed on Pages 11, 108, 142, 147, 169, 179, 198, 202.

**On Sep. 04, 2013, the following changes were made to the Dec. 19, 2012 version of this document:** Errors fixed on Pages 84, 85, 204.

**On Nov. 20, 2013, the following changes were made to the Sep. 04, 2013 version of this document:** Error fixed on Page 129.

**On Aug. 11, 2014, the following changes were made to the Nov. 20, 2013 version of this document:** Error fixed on Page 100.

**On Oct. 10, 2014, the following changes were made to the Aug. 11, 2014 version of this document:** Error fixed on Page 218.

**On Aug. 2, 2016, the following changes were made to the Oct. 10, 2014 version of this document:** Errors fixed on Pages 239 and 241.

interfaced with each other, that is, without power-electronic converters. For instance, a power-electronic converter is required to interface a wind turbine/generator unit, that is, an electromechanical subsystem that generates a variable-frequency/variable-voltage electricity, with the constant-frequency/constant-voltage utility grid, that is, another electromechanical subsystem.

In the technical literature, converters are commonly categorized based on the type of electrical subsystems, that is, AC or DC, that they interface. Thus,

- A DC-to-AC or DC/AC converter interfaces a DC subsystem to an AC subsystem.
- A DC-to-DC or DC/DC converter interfaces two DC subsystems.
- An AC-to-AC or AC/AC converter interfaces two AC subsystems.

Based on the foregoing classification, a DC/AC converter is equivalent to an AC/DC converter. Hence, in this book, the terms DC/AC converter and AC/DC converter are used interchangeably. The conventional diode-bridge rectifier is an example of a DC/AC converter. A DC/AC converter is called a *rectifier* if the flow of average power is from the AC side to the DC side. Alternatively, the converter is called an *inverter* if the average power flow is from the DC side to the AC side. Specific classes of DC/AC converters provide bidirectional power-transfer capability, that is, they can operate either as a rectifier or as an inverter. Other types, for example, the diode-bridge converter, can only operate as a rectifier.

DC/DC converter and AC/AC converter are also referred to as *DC converter* and *AC converter*, respectively. A DC converter can directly interface two DC subsystems, or it can employ an intermediate AC link. In the latter case, the converter is composed of two back-to-back DC/AC converters which are interfaced through their AC sides. Similarly, an AC converter can be direct, for example, the matrix converter, or it can employ an intermediate DC link. The latter type consists of two back-to-back DC/AC converters which are interfaced through their DC sides. This type is also known as *AC/DC/AC converter*, which is widely used in AC motor drives and variable-speed wind-power conversion units.

In this book, we define a *power-electronic converter system* (or a converter system) as a composition of one (or more) power-electronic converter(s) and a control/protection scheme. The link between the converter(s) and the control/protection scheme is established through gating signals issued for semiconductor switches, and also through feedback signals. Thus, the transfer of energy in a converter system is accomplished through appropriate switching of the semiconductor switches by the control scheme, based on the overall desired performance, the supervisory commands, and the feedback from a multitude of system variables.

This book concentrates on modeling and control of a specific class of converter systems, ~~this~~ is, the VSC systems. This class is introduced in Section 1.6.

diodes are extensively used in power-electronic converter circuits as stand-alone components, and/or as integral parts of other switches.

**1.4.1.2 Semicontrollable Switches** The most widely used semicontrollable electronic switch is the thyristor or the silicon-controlled rectifier (SCR). The thyristor is a four-layer semiconductor device that is half- or semicontrollable, since only the instant at which its current conduction starts can be determined by a gating signal, provided that the device is properly voltage biased. However, the current interruption instant of the thyristor is determined by the host electrical circuit. The thyristor has been, and even currently is, the switch of choice for HVDC converters, although in recent years fully controllable switches have also been considered and utilized for HVDC applications.

**1.4.1.3 Fully Controllable Switches** The current conduction and interruption instants of a fully controllable switch can be determined by means of a gating command. Most widely used fully controllable switches include

The most

- *Metal-Oxide-Semiconductor Field-Effect Transistor (MOSFET)*: The MOSFET is a three-layer semiconductor device. Compared to other fully controllable power switches, current and voltage ratings of power MOSFETs are fairly limited. Consequently, the application of power MOSFETs is confined to relatively lower power converters where a high switching frequency is the main requirement.
- *Insulated-Gate Bipolar Transistor (IGBT)*: The IGBT is also a three-layer semiconductor device. The power IGBT has significantly evolved since the early 1990s, in terms of the switching frequency, the current rating, and the voltage rating. At present, it is used for a broad spectrum of applications in electric power systems.
- *Gate-Turn-Off Thyristor (GTO)*: The GTO is structurally a four-layer semiconductor device and can be turned on and off by external gating signals. The GTO requires a relatively large, negative current pulse to turn off. This requirement calls for an elaborate and lossy drive scheme. Among the fully controllable switches, the GTO used to be the switch of choice for high-power applications in the late 1980s and early 1990s. However, it has lost significant ground to the IGBT in the last several years.
- *Integrated Gate-Commutated Thyristor (IGCT)*: The IGCT conceptually and structurally is a GTO switch with mitigated turn-off drive requirements. In addition, the IGCT has a lower on-state voltage drop and can also be switched faster compared to the GTO. In recent years, the IGCT has gained considerable attention for high-power converters due to its voltage/current handling capabilities.

In terms of voltage/current handling capability, the semicontrollable and fully controllable switches are classified as follows:

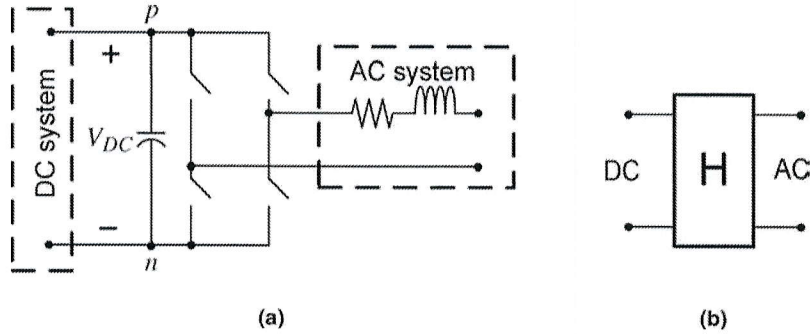


**FIGURE 1.3** (a) Schematic diagram of the full-bridge, single-phase, two-level VSC (or an H-bridge converter). (b) Symbolic representation of the H-bridge converter.

be augmented with an additional half-bridge converter, to represent the fourth leg identical to the other three legs, whose AC terminal is connected to the fourth wire. Various PWM and space-vector modulation techniques for switching the three-phase two-level VSC are described in Ref. [20].

The principles of operation of the half-bridge VSC and the three-phase VSC are discussed in Chapters 2 and 5, respectively.

**1.7.1 Multimodule VSC Systems**

1.1

In high-voltage, high-power VSCs, the switch cell of Figure 1.2(b), which is composed of a fully controllable, unidirectional switch and a diode, may not be able to handle the voltage/current requirements. To overcome this limitation, the switch cells are connected in series and/or in parallel and form a composite switch structure which is called a *valve*. Figure 1.5 shows two valve configurations composed of parallel- and series-connected identical switch cells. In most applications, the existing power semiconductor switches meet current handling requirements. However, in

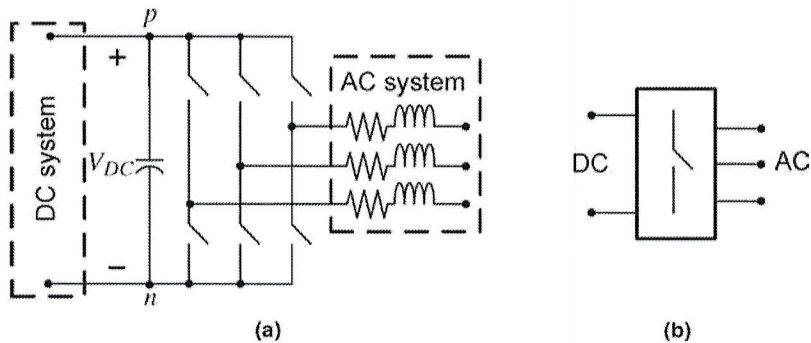


**FIGURE 1.4** (a) Schematic diagram of the three-wire, three-phase, two-level VSC. (b) The symbolic representation of the three-phase VSC.

- Transitions from a conduction state to a blocking state, and vice versa, take place instantly.
- The AC-side current  $i$  is a ripple-free DC quantity.

In the following subsections, we examine the converter switching waveforms on the basis of the abovementioned assumptions. Since the converter operation is different for positive and negative AC-side currents, we study each case separately.

**2.3.2.1 Converter Waveforms for Positive AC-Side Current** Consider the half-bridge converter of Figure 2.1 with a positive AC-side current  $i$ . Assume that  $s_1 = 0$  and thus  $Q_1$  is blocked. Consequently,  $i$  cannot flow through  $D_1$ , since  $i_{D1}$  cannot be negative. For the same reason,  $Q_4$  does not carry  $i$ , although  $s_4 = 1$ . Therefore,  $i$  flows through  $D_4$  and  $V_t = V_n = -V_{DC}/2$ . Now consider a time instant at which  $s_1 = 1$  and  $s_4 = 0$ . In this case,  $Q_1$  conducts while  $Q_4$  is blocked. When  $Q_1$  is on, we have  $V_t = V_p = V_{DC}/2$ , and  $D_4$  is reverse biased. Therefore,  $i$  flows through  $Q_1$ .

The waveforms of the half-bridge converter for positive  $i$  are illustrated in Figure 2.4(a)–(h). As it follows from the foregoing discussion,  $Q_4$  and  $D_1$  play no role in the operation of the converter when  $i$  is positive. The fraction of the switching period  $T_s$  during which  $s_1 = 1$  is called the *duty ratio* and denoted by  $d$ . Under the simplifying assumptions of Section 2.3.2,  $d$  is also equal to the fraction of the switching period during which  $V_t = V_p = V_{DC}/2$ ; however, the latter is not the case if the switching transients are taken into account.<sup>6</sup>

**2.3.2.2 Converter Waveforms for Negative AC-Side Current** It follows from a similar analysis as presented for the case of positive  $i$  that  $Q_1$  and  $D_4$  do not take part in the converter operation when  $i$  is negative. In this case, when  $s_4 = 1$ ,  $Q_4$  conducts and  $V_t = V_n = -V_{DC}/2$ . Alternatively, when  $s_4 = 0$ , the AC-side current passes through  $D_1$  and  $V_t = V_p = V_{DC}/2$ . The duty ratio,  $d$ , is defined in the same way as in the case of the positive AC-side current. Figure 2.5(a)–(h) illustrates the waveforms of the half-bridge converter for negative  $i$ .

## 2.4 CONVERTER SWITCHED MODEL

To employ the half-bridge converter as a component of a larger system, we need to identify the characteristics of the converter as observed from its terminals. The switched model of the half-bridge converter introduces the relationships among the converter terminal voltages and currents. A comparison between Figures 2.4 and 2.5 indicates that in a switch cell the waveform of the current through the transistor, or that through the diode, depends on the direction of the converter AC-side current. However, since  $i_p = i_{Q1} - i_{D1}$  and  $i_n = -i_{Q4} + i_{D4}$ , the waveform of the switch cell

<sup>6</sup>We will show this in Section 2.6.

$Q_1$  carries  $i$  (Fig. 2.14(d)), and

$$V'_t = V_p - r_{on}i - V_d. \quad (2.32)$$

Note that the term  $r_{on}i + V_d$  is considerably smaller than  $V_p$  and therefore  $V'_t \approx V_p = V_{DC}/2$ , as Figure 2.14(c) indicates. At  $t = dT_s$ , the gating command of  $Q_1$  is removed and  $i_{Q1}$  rapidly drops to its tailing current level (Fig. 2.14(d)). Therefore,  $D_4$  starts conducting, and  $i_{D4}$  increases rapidly (Fig. 2.14(e)). The tailing current process lasts for  $t_{tc}$  until the whole tailing current charge of  $Q_{tc}$  is removed from the transistor. During the tailing current process, the following equation holds:

$$\begin{aligned} V'_t &= V_n - r_{on}i_{D4} - V_d \\ &= V_n - r_{on}(i - i_{Q1}) - V_d, \end{aligned} \quad (2.33)$$

and  $V'_t \approx -V_{DC}/2$  (Fig. 2.14(c)). At  $t = dT_s + t_{tc}$ ,  $i_{Q1}$  becomes zero and  $i_{D4} = i$ , as Figure 2.14(e) illustrates. From  $t = dT_s + t_{tc}$  to  $T_s$ , the whole AC-side current is carried by  $D_4$ , and we have

$$V'_t = V_n - r_{on}i - V_d, \quad (2.34)$$

and  $V'_t \approx -V_{DC}/2$ , as Figure 2.14(c) shows.

The average of the AC-side terminal voltage is

$$\begin{aligned} \overline{V'_t} &= \frac{1}{T_s} \int_0^{T_s} V'_t(\tau) d\tau \\ &= \frac{1}{T_s} \left( \int_0^{t_{rr}} V'_t d\tau + \int_{t_{rr}}^{dT_s} V'_t d\tau + \int_{dT_s}^{dT_s+t_{tc}} V'_t d\tau + \int_{dT_s+t_{tc}}^{T_s} V'_t d\tau \right), \end{aligned} \quad (2.35)$$

where  $V'_t$ , for each time interval, is obtained from (2.31) to (2.34), respectively. Substituting for  $V'_t$  in (2.35), based on (2.31)–(2.34), knowing that  $\int_0^{t_{rr}} i_{D4}(\tau) d\tau = -Q_{rr}$  and  $\int_{dT_s}^{dT_s+t_{tc}} i_{Q1} d\tau = Q_{tc}$ , and rearranging the result, we conclude that

$$\begin{aligned} \overline{V'_t} &= m \frac{V_{DC}}{2} - V_e - r_e i \\ &= \overline{V}_t - V_e - r_e i, \quad \text{for } i > 0, \end{aligned} \quad (2.36)$$

where  $\overline{V}_t = m V_{DC}/2$  based on (2.26), and

$$V_e = V_d - \left( \frac{Q_{rr} + Q_{tc}}{T_s} \right) r_{on} + V_{DC} \left( \frac{t_{rr}}{T_s} \right), \quad (2.37)$$

$$r_e = \left( 1 - \frac{t_{rr}}{T_s} \right) r_{on}. \quad (2.38)$$

step function and  $V_s$  is a DC voltage, a proportional-integral (PI) compensator of the generic form  $K(s) = (k_p s + k_i)/s$  is sufficient for the control. The integral term of the compensator guarantees that  $i$  tracks  $i_{ref}$ , with zero steady-state error, in spite of the disturbance  $V_s$ .

As understood from Figure 3.3, if  $K(s) = (k_p s + k_i)/s$ , the control system loop gain is

$$\ell(s) = \left( \frac{k_p}{Ls} \right) \left( \frac{s + \frac{k_i}{k_p}}{s + \frac{R+r_{on}}{L}} \right). \quad (3.3)$$

Based on the block diagrams of Figures 3.2 and 3.3, the open-loop half-bridge converter has a stable pole at  $p = -(R + r_{on})/L$ . Typically, this pole is fairly close to the origin and corresponds to a slow natural response. To improve the open-loop frequency response, the pole can be canceled by the zero of the PI compensator. Thus, choosing  $k_i/k_p = (R + r_{on})/L$  and  $k_p/L = 1/\tau_i$ , where  $\tau_i$  is the desired time constant of the closed-loop system, one obtains the closed-loop transfer function

$$G_i(s) = \frac{\mathbf{I}(s)}{\mathbf{I}_{ref}(s)} = \frac{1}{\tau_i s + 1}, \quad (3.4)$$

which is a first-order transfer function with the unity gain.  $\tau_i$  should be made small for a fast current-control response, but adequately large such that  $1/\tau_i$ , that is, the bandwidth of the closed-loop control system, is considerably smaller, for example, 10 times smaller, than the switching frequency of the half-bridge converter (expressed in rad/s). Depending on the requirements of a specific application and the converter switching frequency,  $\tau_i$  is typically selected in the range of 0.5–5 ms.

Example 3.1 illustrates the performance of the current-controlled half-bridge converter in tracking a step command.

### EXAMPLE 3.1 Closed-Loop Response of the Half-Bridge Converter

Consider the half-bridge converter of Figure 3.1 with parameters  $L = 690 \mu\text{H}$ ,  $R = 5 \text{ m}\Omega$ ,  $r_{on} = 0.88 \text{ m}\Omega$ ,  $V_d = 1.0 \text{ V}$ ,  $V_{DC}/2 = 600 \text{ V}$ ,  $V_s = 400 \text{ V}$ , and  $f_s = 1620 \text{ Hz}$ . To achieve a closed-loop time constant of 5 ms, the compensator parameters are chosen as  $k_p = 0.138 \Omega$  and  $k_i = 1.176 \Omega/\text{s}$ .

Initially, the half-bridge converter system is in a steady state and  $i = 0$ . The current command,  $i_{ref}$ , is first changed from 0 to 1000 A, at  $t = 0.1 \text{ s}$ , and then changed from 1000 to  $-1000 \text{ A}$ , at  $t = 0.2 \text{ s}$ . These correspond to changes in the AC-side power from 0 to 400 kW and from 400 to  $-400 \text{ kW}$ , respectively. Figure 3.4(a)–(d) shows the half-bridge converter response to the step changes in  $i_{ref}$ . Figure 3.4(a) shows the compensator response to the command changes. The response of the compensator output  $u$  is equivalent to that of the AC-side terminal voltage  $V_t$ , required for the command tracking.  $u$  is then translated into the modulating waveform  $m$  (Fig. 3.4(b)), which is rendered to the converter PWM scheme. As expected, the step response of  $i$  is a first-order exponential

a very small closed-loop time constant may not be possible due to practical limitations/requirements. For example, while a closed-loop current controller with a time constant of  $\tau_i = 2$  ms is considered as being reasonably fast for most high-power converter systems, it tracks a 60 Hz sinusoidal command with an amplitude attenuation of 20% and a phase delay of  $37^\circ$ .

Example 3.5 illustrates the sinusoidal command following performance of the half-bridge converter system if a PI compensator is used.

**EXAMPLE 3.5 Sinusoidal Command Following with PI Compensator**

Consider the half-bridge converter of Figure 3.1, in conjunction with the control scheme of Figure 3.6, with the following parameters:  $L = 690 \mu\text{H}$ ,  $R = 5 \text{ m}\Omega$ ,  $r_{on} = 0.88 \text{ m}\Omega$ ,  $V_d = 1.0 \text{ V}$ ,  $V_{DC}/2 = 600 \text{ V}$ , and  $f_s = 3420 \text{ Hz}$ . The compensator parameters are  $k_p = 0.345 \Omega$  and  $k_i = 2.94 \Omega/\text{s}$ , which correspond to  $\tau_i = 2\text{ms}$ . The transfer function of the feed-forward filter is  $G_{ff}(s) = 1/(8 \times 10^{-6}s + 1)$ .

Let us assume that  $V_s = 400 \cos(377t - \frac{\pi}{2}) \text{ V}$  and that we intend to deliver 200 kW to the AC system, at unity power factor. Thus, the current command  $i_{ref} = 1000 \cos(377t - \frac{\pi}{2}) \text{ A}$  must be tracked by the closed-loop converter system. Figure 3.15 shows the system closed-loop response to  $i_{ref}$  when a PI compensator is employed. As Figure 3.15 illustrates,  $i(t)$  is about  $37^\circ$  delayed with respect to  $i_{ref}(t)$  and  $V_s(t)$ . Moreover, the amplitude of  $i$  is only about 800 A. Consequently, rather than 200 kW at unity power factor, 128 kW and 96 kVAr are delivered to the AC-side source.

To further investigate the mechanism of the time-varying command tracking, consider the closed-loop control system of Figure 3.16 with the transfer function

$$\frac{I(s)}{I_{ref}(s)} = G_i(s) = \frac{\ell(s)}{1 + \ell(s)}, \tag{3.9}$$

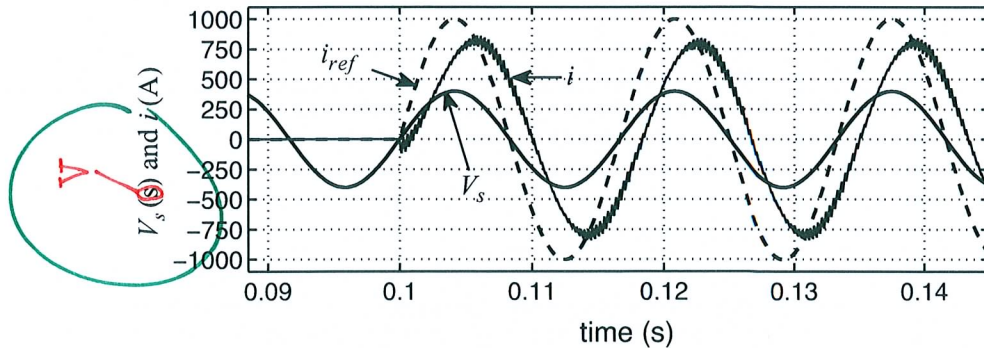


**FIGURE 3.15** Steady-state error in phase and amplitude of the current when PI compensator is employed; Example 3.5.

adequately larger than the frequency of the command signal. In this approach, no attempt is usually made to include the unstable poles of the command signal in the compensator. Consequently, the tracking will not be perfect and a steady-state error, although small, is inevitable. The design procedure is almost the same in both methods and illustrated by Example 3.6.

### EXAMPLE 3.6 Sinusoidal Command Following with a Modified Compensator

Consider the half-bridge converter of Example 3.5 and the control block diagram of Figure 3.6. Let us assume that  $i_{ref}$  is required to be tracked with zero steady-state error and that a closed-loop bandwidth of about 3500 rad/s (i.e., about 9 times  $\omega_0$ ) is desired.

To satisfy the zero steady-state error requirement, we include a pair of complex-conjugate poles in the compensator, at  $s = \pm 377j$  rad/s. Thus, a candidate compensator is  $K(s) = (s^2 + (377)^2)^{-1} H(s)$ , where  $H(s) = h(N(s)/D(s))$  is a rational fraction of the polynomials  $N(s)$  and  $D(s)$ , and  $h$  is a constant.<sup>2</sup> The compensator zeros and the other poles (if required) must be located in the  $s$  plane such that the closed-loop system is stable, a reasonable phase margin is achieved, and the switching ripple content of the control signal  $u$  is low. The compensator can be designed based on either the root-locus method or the frequency-response approach. For this example, we adopt the frequency-response method (also known as the *loop shaping*).

If  $H(j\omega) = 1$ , that is,  $K(j\omega) = [-\omega^2 + (377)^2]^{-1}$ , the magnitude and phase plots of  $\ell(j\omega) = K(j\omega)G(j\omega) = K(j\omega)[jL\omega + (R + r_{on})]^{-1}$  assume the shapes shown by dashed lines in Figure 3.17. It is observed that at very low frequencies  $\ell(j\omega)$  has a constant magnitude, and the phase delay is insignificant. However, due to the open-loop pole  $s = -(R + r_{on})/L$ , the magnitude starts to roll off at about  $\omega = 8.52$  rad/s. The pole also results in a phase drop with a slope of  $-45^\circ/\text{dec}$ , such that the phase settles at  $-90^\circ$  for frequencies larger than 85 rad/s. At  $\omega = 377$  rad/s, that is, the resonance frequency of the complex-conjugate poles, the loop-gain magnitude peaks to infinity but continues to roll off with a slope of  $-60$  dB/dec. The resonance also results in a  $-180^\circ$  phase delay, such that the loop-gain phase drops to  $-270^\circ$ , for frequencies larger than 377 rad/s.

To achieve a stable closed-loop system, one must ensure that the loop-gain phase at the gain crossover frequency is larger than  $-180^\circ$ , by a value that is referred to as the *phase margin*. The gain crossover frequency, denoted by  $\omega_c$ , is the frequency at which the loop-gain magnitude becomes unity (0 dB) [37]. On the other hand, the gain crossover frequency and the  $-3$  dB bandwidth of the closed-loop system, denoted by  $\omega_b$ , are closely correlated, such that, in general,  $\omega_b$  satisfies the inequality  $\omega_c < \omega_b < 2\omega_c$  and can be approximated as  $\omega_b \approx 1.5\omega_c$ . Therefore,  $\omega_c$  is imposed if a certain value is required for  $\omega_b$ . In this

<sup>2</sup> $N(s)$  and  $D(s)$  are arranged such that the coefficients of their highest order terms are unity.

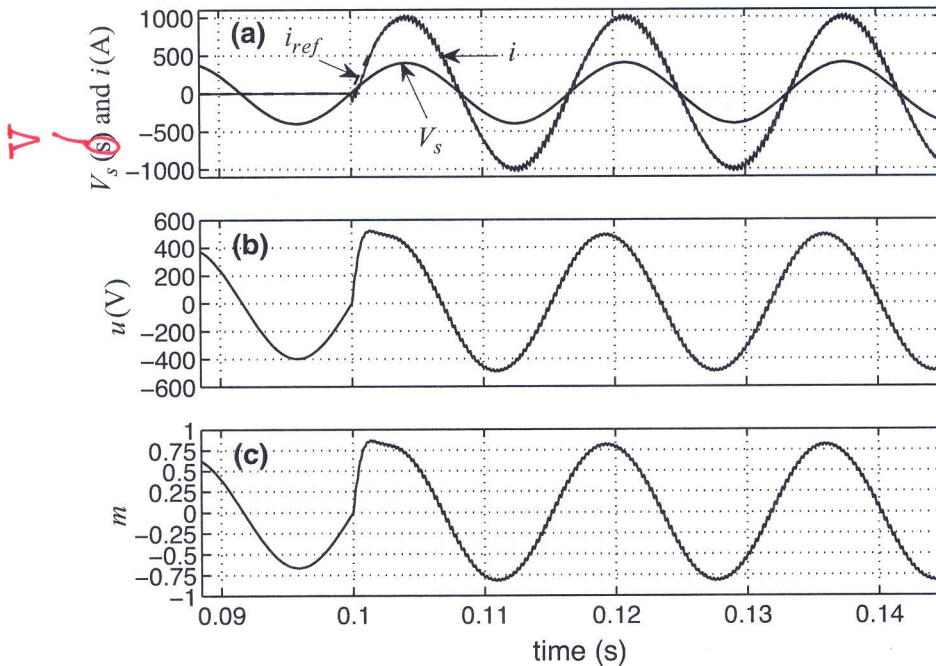


FIGURE 3.20 Response of the half-bridge converter to a sinusoidal command, based on the compensator of (3.19); Example 3.6.

Figures

Figure 3.20(a) illustrates that  $i(t)$  rapidly reaches and tracks  $i_{ref}$ , without amplitude or phase-angle errors. Figure 3.20(b) and (c) shows the waveforms of the compensator output (control signal) and the modulating signal, respectively. It is observed that the switching ripples of these signals are small.

look at

3.1, 3.5, and 3.6

A comparison of the corresponding results in Examples 3.5 and 3.6 shows that the compensator structure is significantly more complex for sinusoidal command tracking than that for the DC command tracking. As noted in Example 3.5, a PI compensator is sufficient to ensure DC command following with a satisfactory performance. However, as indicated by Example 3.6, a more elaborate compensator is required to track a sinusoidal command, with a high degree of fidelity. Furthermore, the control loop must be designed for a much wider bandwidth in case of sinusoidal command following.

In three-phase VSC systems, we are often interested in tracking a sinusoidal command, rapidly and with small steady-state errors. We also need to stipulate rapid changes in the amplitude and/or the phase of the commands. Therefore, the control design is noticeably simplified if we can transform the problem of sinusoidal command tracking to a DC command tracking problem. The reference-frame theory and the techniques introduced in Chapter 4 are instrumental to that end.

Examples 3.5 and 3.6

3.1

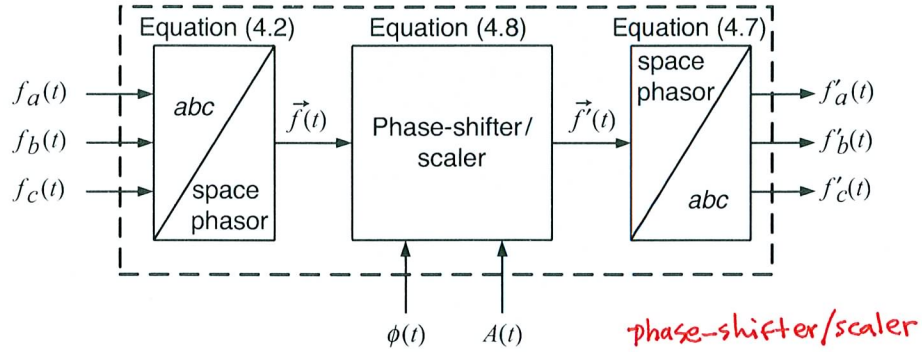


FIGURE 4.5 Block diagram of the modified space-phasor phase shifter/scaler.

AC-side terminal voltage,  $V_{t-abc}$ , relative to those of the AC system voltage,  $V_{s-abc}$  [46, 47]. Thus,  $\phi(t)$  ( $A(t)$ ) is commanded by a (another) feedback loop that processes the error between the real power (reactive power) and its respective reference value, to regulate the real power (reactive power). The output of the space-phasor phase-shifter/scaler corresponds to the terminal voltage to be reproduced by the VSC and is delivered to the VSC pulse-width modulation (PWM) switching scheme.

Example 4.1 illustrates the operation of the space-phasor phase-shifter/scaler of Figure 4.4.

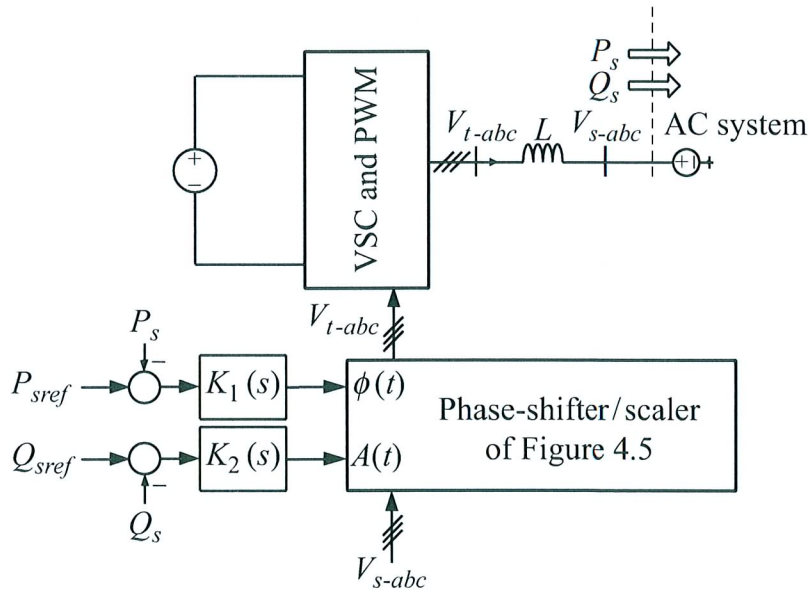


FIGURE 4.6 Block diagram of voltage-controlled VSC system.

**TABLE 4.1** Positive- and Negative-Sequence Harmonics

Positive-Sequence Harmonic $\vec{f}_n(t) = \hat{f}_n e^{jn\omega t}$	Negative-Sequence Harmonic $\vec{f}_n(t) = \hat{f}_n e^{-jn\omega t}$
$n = 1$	$n = 2$
4	5
7	8
10	11
13	14
16 →	17
19	20
22	23
25	26 ← 2.9
28	32
31	

we identify three classes of three-phase systems: symmetrical and decoupled, symmetrical and coupled, and asymmetrical.

**4.3.1 Decoupled Symmetrical Three-Phase Systems**

Consider the three-phase system of Figure 4.13 in which each phase of the output  $y_{abc}$  is controlled by the corresponding phase of the input  $u_{abc}$ . The system of Figure 4.13 is composed of three decoupled identical subsystems. The system is symmetrical since the input/output relationships of the three phases retain their original expressions if

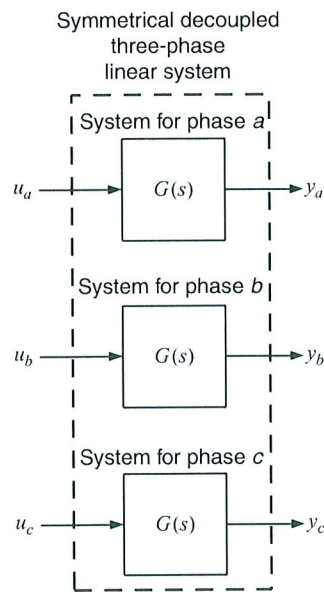


**FIGURE 4.13** Block diagram of a symmetrical, decoupled, linear, three-phase system.

index  $a$  is replaced by  $b$ , index  $b$  is replaced by  $c$ , and index  $c$  is replaced by  $a$  in the phase equations. Let the input/output relationship of each subsystem be described by a transfer function,  $G(s)$ , as

$$\begin{aligned} Y_a(s) &= G(s)U_a(s), \\ Y_b(s) &= G(s)U_b(s), \\ Y_c(s) &= G(s)U_c(s), \end{aligned} \quad (4.16)$$

where  $G(s) = (k_m s^m + k_{m-1} s^{m-1} + \dots + k_0)/(s^n + l_{n-1} s^{n-1} + \dots + l_0)$  is a rational transfer function; it can be verified based on (4.16) that the system of Figure 4.13 is symmetrical. The time-domain equations of the three-phase system are

$$\frac{d^n y_a}{dt^n} + l_{n-1} \frac{d^{n-1} y_a}{dt^{n-1}} + \dots + l_0 y_a = k_m \frac{d^m u_a}{dt^m} + k_{m-1} \frac{d^{m-1} u_a}{dt^{m-1}} + \dots + k_0 u_a, \quad (4.17)$$

$$\frac{d^n y_b}{dt^n} + l_{n-1} \frac{d^{n-1} y_b}{dt^{n-1}} + \dots + l_0 y_b = k_m \frac{d^m u_b}{dt^m} + k_{m-1} \frac{d^{m-1} u_b}{dt^{m-1}} + \dots + k_0 u_b, \quad (4.18)$$

$$\frac{d^n y_c}{dt^n} + l_{n-1} \frac{d^{n-1} y_c}{dt^{n-1}} + \dots + l_0 y_c = k_m \frac{d^m u_c}{dt^m} + k_{m-1} \frac{d^{m-1} u_c}{dt^{m-1}} + \dots + k_0 u_c. \quad (4.19)$$

Multiplying both sides of (4.17), (4.18), and (4.19), respectively, by  $\frac{2}{3}e^{j0}$ ,  $\frac{2}{3}e^{j\frac{2\pi}{3}}$ , and  $\frac{2}{3}e^{j\frac{4\pi}{3}}$ , one obtains

$$\begin{aligned} &\frac{d^n}{dt^n} \left( \frac{2}{3} e^{j0} y_a \right) + l_{n-1} \frac{d^{n-1}}{dt^{n-1}} \left( \frac{2}{3} e^{j0} y_a \right) + \dots + l_0 \left( \frac{2}{3} e^{j0} y_a \right) \\ &= k_m \frac{d^m}{dt^m} \left( \frac{2}{3} e^{j0} \cancel{y_a} \right) + k_{m-1} \frac{d^{m-1}}{dt^{m-1}} \left( \frac{2}{3} e^{j0} \cancel{y_a} \right) + \dots + k_0 \left( \frac{2}{3} e^{j0} \cancel{y_a} \right), \end{aligned} \quad (4.20)$$

*Handwritten red annotations:  $u_a$  under  $\cancel{y_a}$  in each term.*

$$\begin{aligned} &\frac{d^n}{dt^n} \left( \frac{2}{3} e^{j\frac{2\pi}{3}} y_b \right) + l_{n-1} \frac{d^{n-1}}{dt^{n-1}} \left( \frac{2}{3} e^{j\frac{2\pi}{3}} y_b \right) + \dots + l_0 \left( \frac{2}{3} e^{j\frac{2\pi}{3}} y_b \right) \\ &= k_m \frac{d^m}{dt^m} \left( \frac{2}{3} e^{j\frac{2\pi}{3}} \cancel{y_b} \right) + k_{m-1} \frac{d^{m-1}}{dt^{m-1}} \left( \frac{2}{3} e^{j\frac{2\pi}{3}} \cancel{y_b} \right) + \dots + k_0 \left( \frac{2}{3} e^{j\frac{2\pi}{3}} \cancel{y_b} \right), \end{aligned} \quad (4.21)$$

*Handwritten red annotations:  $u_b$  under  $\cancel{y_b}$  in each term.*

$$\begin{aligned}
& \frac{d^n}{dt^n} \left( \frac{2}{3} e^{j\frac{4\pi}{3}} y_c \right) + l_{n-1} \frac{d^{n-1}}{dt^{n-1}} \left( \frac{2}{3} e^{j\frac{4\pi}{3}} y_c \right) + \cdots + l_0 \left( \frac{2}{3} e^{j\frac{4\pi}{3}} y_c \right) \\
& = k_m \frac{d^m}{dt^m} \left( \frac{2}{3} e^{j\frac{4\pi}{3}} y_c \right) + k_{m-1} \frac{d^{m-1}}{dt^{m-1}} \left( \frac{2}{3} e^{j\frac{4\pi}{3}} y_c \right) + \cdots + k_0 \left( \frac{2}{3} e^{j\frac{4\pi}{3}} y_c \right).
\end{aligned} \tag{4.22}$$

Adding the corresponding sides of (4.20), (4.21), and (4.22), and using (4.2), one concludes that

$$\frac{d^n}{dt^n} \vec{y} + l_{n-1} \frac{d^{n-1}}{dt^{n-1}} \vec{y} + \cdots + l_0 \vec{y} = k_m \frac{d^m}{dt^m} \vec{u} + k_{m-1} \frac{d^{m-1}}{dt^{m-1}} \vec{u} + \cdots + k_0 \vec{u}. \tag{4.23}$$

Equation (4.23) represents the system of Figure 4.13 in the space-phasor domain. It is noted that the system input–output relationship in the space-phasor domain has the same form as that for each subsystem in the  $abc$ -frame. Equation (4.23) provides a compact representation of the original three-phase system. It can be observed that (4.23) possesses the same form as each of (4.17), (4.18), and (4.19). Therefore, the space-phasor equations of a symmetrical, decoupled, linear, three-phase system can be conveniently derived by replacing the time-domain variables with the corresponding space-phasor variables in any set of equations corresponding to the three phases.

The foregoing procedure to transform the differential equations of a three-phase system to space-phasor domain can also be readily applied to state-space equations, as illustrated in Example 4.4.

#### EXAMPLE 4.4 Space-Phasor State-Space Equations of a Three-Phase Circuit

Figure 4.14 illustrates a simplified circuit diagram of a current-controlled three-phase VSC system of which each phase is interfaced with the corresponding phase of an AC system. The AC system is represented by a voltage source  $v_{sabc}$  in series with three decoupled inductors, one per phase. The inductance of each inductor is  $L_s$ . In the circuit of Figure 4.14,  $v_{abc}$  signifies the voltage of the point of common coupling (PCC), and  $i_{sabc}$  and  $i_{abc}$  represent the AC system current and the VSC current, respectively. Since, in practice,  $i_{abc}$  contains harmonic components, the capacitors  $C$  are used to provide bypass paths for the harmonics and prevent them from penetrating into the AC system. It is assumed that the fundamental component of  $i_{abc}$  can be controlled by a PWM scheme. This, in turn, enables the control of real and reactive power that the VSC system delivers to the AC system.

Based on the aforementioned description of the circuit of Figure 4.14,  $i_{abc}$  is the control variable whereas  $v_{abc}$  and  $i_{sabc}$  are the state variables. Since there is no control over  $v_{sabc}$ , it is regarded as the disturbance input. Depending on

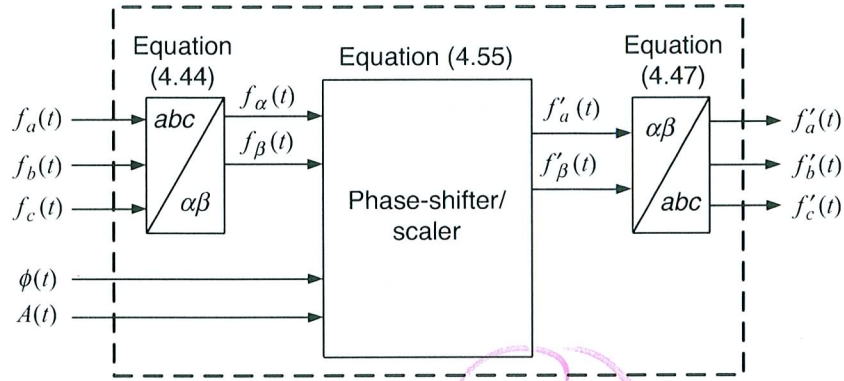


**FIGURE 4.22** Block diagram of a space-phasor phase-shifter/scaler in  $\alpha\beta$ -frame, equivalent to Figure 4.5

↑  
shifter

$i_\alpha - ji_\beta$ , and obtain

$$P(t) = \frac{3}{2} [v_\alpha(t)i_\alpha(t) + v_\beta(t)i_\beta(t)] \quad (4.56)$$

and

$$Q(t) = \frac{3}{2} [-v_\alpha(t)i_\beta(t) + v_\beta(t)i_\alpha(t)]. \quad (4.57)$$

#### 4.5.4 Control in $\alpha\beta$ -Frame

Figure 4.24 illustrates the generic control block diagram of a three-phase VSC system in  $\alpha\beta$ -frame. The control plant may consist of three-phase electric machines, VSCs,

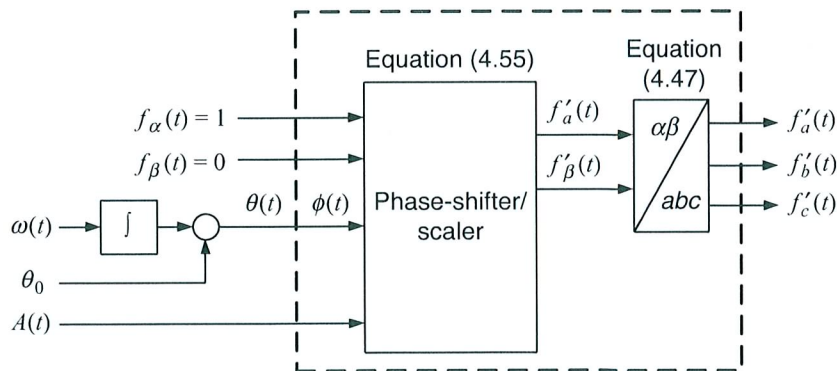


**FIGURE 4.23** Block diagram of a controllable-frequency/amplitude three-phase signal generator in  $\alpha\beta$ -frame, equivalent to Figure 4.10.

**EXAMPLE 4.7 Space-Phasor Equations of Three Mutually Coupled Inductors**

Consider an asymmetrical three-phase system governed by the following matrix equation:

$$\begin{bmatrix} v_a \\ v_b \\ v_c \end{bmatrix} = \begin{bmatrix} L_s & M_{ab} & M_{ac} \\ M_{ab} & L_s & M_{bc} \\ M_{ac} & M_{bc} & L_s \end{bmatrix} \frac{d}{dt} \begin{bmatrix} i_a \\ i_b \\ i_c \end{bmatrix}, \quad (4.60)$$

which represents three mutually coupled inductors with unequal mutual inductances. To derive the  $\alpha\beta$ -frame equations, based on (4.47), the  $abc$ -frame voltage and current vectors are expressed in  $\alpha\beta$ -frame. Hence,

$$\begin{aligned} \mathbf{C}^T \begin{bmatrix} v_\alpha \\ v_\beta \end{bmatrix} &= \begin{bmatrix} L_s & M_{ab} & M_{ac} \\ M_{ab} & L_s & M_{bc} \\ M_{ac} & M_{bc} & L_s \end{bmatrix} \frac{d}{dt} \left( \mathbf{C}^T \begin{bmatrix} i_\alpha \\ i_\beta \end{bmatrix} \right) \\ &= \begin{bmatrix} L_s & M_{ab} & M_{ac} \\ M_{ab} & L_s & M_{bc} \\ M_{ac} & M_{bc} & L_s \end{bmatrix} \mathbf{C}^T \frac{d}{dt} \begin{bmatrix} i_\alpha \\ i_\beta \end{bmatrix}, \end{aligned} \quad (4.61)$$

where  $\mathbf{C}$  is given by (4.45). Premultiplying both sides of (4.61) by  $(2/3)\mathbf{C}$  and using the identity (4.53) at the left-hand side of the resultant, we deduce

$$\begin{bmatrix} v_\alpha \\ v_\beta \end{bmatrix} = \frac{2}{3} \mathbf{C} \begin{bmatrix} L_s & M_{ab} & M_{ac} \\ M_{ab} & L_s & M_{bc} \\ M_{ac} & M_{bc} & L_s \end{bmatrix} \mathbf{C}^T \frac{d}{dt} \begin{bmatrix} i_\alpha \\ i_\beta \end{bmatrix}. \quad (4.62)$$

Substituting in (4.62) for  $\mathbf{C}$  and  $\mathbf{C}^T$ , based on (4.45), one deduces

$$\begin{bmatrix} v_\alpha \\ v_\beta \end{bmatrix} = \frac{2}{3} \begin{bmatrix} \frac{3}{2}L_s - (M_{ab} + M_{ac}) + \frac{1}{2}M_{bc} & \frac{\sqrt{3}}{2}(M_{ab} - M_{ac}) \\ \frac{\sqrt{3}}{2}(M_{ab} - M_{ac}) & \frac{3}{2}(L_s - M_{bc}) \end{bmatrix} \frac{d}{dt} \begin{bmatrix} i_\alpha \\ i_\beta \end{bmatrix}. \quad (4.63)$$

Equation (4.63) indicates that  $v_\alpha$  and  $v_\beta$  ~~are~~ <sup>are</sup> functions of both  $i_\alpha$  and  $i_\beta$ , through different transfer functions. However, if the mutual inductances are identical and equal to  $M$ , the three inductors constitute a symmetrical (coupled) three-phase system, and (4.63) is simplified to

$$\begin{bmatrix} v_\alpha \\ v_\beta \end{bmatrix} = \begin{bmatrix} (L_s - M) & 0 \\ 0 & (L_s - M) \end{bmatrix} \frac{d}{dt} \begin{bmatrix} i_\alpha \\ i_\beta \end{bmatrix}, \quad (4.64)$$

To highlight the usefulness of the transformation given by (4.65), assume that  $\vec{f}$  has the following general form:

$$\vec{f}(t) = f_\alpha + jf_\beta = \hat{f}(t)e^{j[\theta_0 + \int \omega(\tau)d\tau]},$$

where  $\omega(t)$  is the (time-varying) frequency and  $\theta_0$  is the initial phase angle of the three-phase signal corresponding to  $\vec{f}(t)$ . If  $\varepsilon(t)$  is chosen as

$$\varepsilon(t) = \varepsilon_0 + \int \omega(\tau)d\tau,$$

then based on (4.65) the  $dq$ -frame representation of  $\vec{f}(t)$  becomes

$$f_d + jf_q = \hat{f}(t)e^{j(\theta_0 - \varepsilon_0)},$$

which is stationary and, therefore, the constituents of its corresponding three-phase signal are DC quantities. Note that  $\theta(t)$  and  $\varepsilon(t)$  are not necessarily equal, but  $d\theta(t)/dt = d\varepsilon(t)/dt$  must be ensured.

To better describe the  $dq$ -frame transformation, let us rewrite (4.66) as

$$\vec{f} = f_d(1 + 0 \cdot j)e^{j\varepsilon(t)} + f_q(0 + 1 \cdot j)e^{j\varepsilon(t)}. \quad (4.67)$$

An interpretation of (4.67) is that the vector  $\vec{f}$  is represented by its components, that is,  $f_d$  and  $f_q$ , in an orthogonal coordinate system whose axes are along the unit vectors  $(1 + 0 \cdot j)e^{j\varepsilon(t)}$  and  $(0 + 1 \cdot j)e^{j\varepsilon(t)}$ . In turn,  $(1 + 0 \cdot j)$  and  $(0 + 1 \cdot j)$  are the unit vectors along the  $\alpha$ -axis and the  $\beta$ -axis of the  $\alpha\beta$ -frame, respectively. Therefore, as illustrated in Figure 4.26, one can consider  $\vec{f}$  as a vector represented by the components  $f_d$  and  $f_q$  in a coordinate system that is rotated by  $\varepsilon(t)$  with respect to the  $\alpha\beta$ -frame. We refer to this rotated coordinate system as a  $dq$ -frame. For the reason given above, the  $dq$ -frame is also known as *rotating reference frame*, in the technical literature. Usually, the rotational speed of the  $dq$ -frame is selected to be equal to that of  $\vec{f}$ .

Based on the Euler's identity  $e^{j(\cdot)} = \cos(\cdot) + j \sin(\cdot)$ , (4.65) can be written as

$$\begin{bmatrix} f_d(t) \\ f_q(t) \end{bmatrix} = \mathbf{R}[\varepsilon(t)] \begin{bmatrix} f_\alpha(t) \\ f_\beta(t) \end{bmatrix}, \quad (4.68)$$

where

$$\mathbf{R}[\varepsilon(t)] = \begin{bmatrix} \cos \varepsilon(t) & \sin \varepsilon(t) \\ -\sin \varepsilon(t) & \cos \varepsilon(t) \end{bmatrix}. \quad (4.69)$$

A direct transformation from the  $abc$ -frame to the  $dq$ -frame can be obtained by substitution of  $[f_\alpha \ f_\beta]^T$  from (4.44) in (4.68), as

$$\begin{bmatrix} f_d(t) \\ f_q(t) \end{bmatrix} = \frac{2}{3} \mathbf{T}[\varepsilon(t)] \begin{bmatrix} f_a(t) \\ f_b(t) \\ f_c(t) \end{bmatrix}, \quad (4.73)$$

where

$$\mathbf{T}[\varepsilon(t)] = \mathbf{R}[\varepsilon(t)]\mathbf{C} = \begin{bmatrix} \cos[\varepsilon(t)] \cos\left[\varepsilon(t) - \frac{2\pi}{3}\right] \cos\left[\varepsilon(t) - \frac{4\pi}{3}\right] \\ \sin[\varepsilon(t)] \sin\left[\varepsilon(t) - \frac{2\pi}{3}\right] \sin\left[\varepsilon(t) - \frac{4\pi}{3}\right] \end{bmatrix} \quad (4.74)$$

Similarly, a direct transformation from the  $dq$ -frame to the  $abc$ -frame can be obtained by substituting for  $[f_\alpha \ f_\beta]^T$  from (4.70) in (4.47) as

$$\begin{bmatrix} f_a(t) \\ f_b(t) \\ f_c(t) \end{bmatrix} = \mathbf{T}[\varepsilon(t)]^T \begin{bmatrix} f_d(t) \\ f_q(t) \end{bmatrix}, \quad (4.75)$$

where

$$\mathbf{T}[\varepsilon(t)]^T = \mathbf{C}^T \mathbf{R}[-\varepsilon(t)] = \begin{bmatrix} \cos[\varepsilon(t)] & \sin[\varepsilon(t)] \\ \cos\left[\varepsilon(t) - \frac{2\pi}{3}\right] & \sin\left[\varepsilon(t) - \frac{2\pi}{3}\right] \\ \cos\left[\varepsilon(t) - \frac{4\pi}{3}\right] & \sin\left[\varepsilon(t) - \frac{4\pi}{3}\right] \end{bmatrix}. \quad (4.76)$$

Based on Figure 4.26, one deduces

$$\widehat{f}(t) = \sqrt{f_d^2(t) + f_q^2(t)}, \quad (4.77)$$

$$\cos[\delta(t)] = \frac{f_d(t)}{\widehat{f}(t)} = \frac{f_d(t)}{\sqrt{f_d^2(t) + f_q^2(t)}}, \quad (4.78)$$

$$\sin[\delta(t)] = \frac{f_q(t)}{\widehat{f}(t)} = \frac{f_q(t)}{\sqrt{f_d^2(t) + f_q^2(t)}}, \quad (4.79)$$

$$\theta(t) = \varepsilon(t) + \delta(t). \quad (4.80)$$

**EXAMPLE 4.8** *dq*-Frame Model of the Three-Phase System of Example 4.4

Consider the circuit of Figure 4.14 for which the space-phasor equations are given by (4.30) and (4.31). Substituting for  $\vec{v} = v_{dq}e^{j\epsilon(t)}$ ,  $\vec{i} = i_{dq}e^{j\epsilon(t)}$ , and  $\vec{i}_s = i_{sdq}e^{j\epsilon(t)}$  in (4.30), we obtain

$$C \frac{d}{dt} (v_{dq}e^{j\epsilon(t)}) = (i_{dq}e^{j\epsilon(t)}) - (i_{sdq}e^{j\epsilon(t)}), \quad (4.85)$$

where  $f_{dq} = f_d + jf_q$ . Equation (4.85) can be rewritten as

$$\left( C \frac{dv_{dq}}{dt} \right) e^{j\epsilon(t)} + \underbrace{(j\omega v_{dq})}_{jC\omega v_{dq}} e^{j\epsilon(t)} = (i_{dq}) e^{j\epsilon(t)} - (i_{sdq}) e^{j\epsilon(t)}, \quad (4.86)$$

where

$$\frac{d\epsilon}{dt} = \omega(t). \quad (4.87)$$

Eliminating  $e^{j\epsilon(t)}$  from both sides of (4.86) and decomposing the resultant into the real and imaginary parts, we conclude that

$$C \frac{dv_d}{dt} = C\omega(t)v_q + i_d - i_{sd}, \quad (4.88)$$

$$C \frac{dv_q}{dt} = -C\omega(t)v_d + i_q - i_{sq}. \quad (4.89)$$

Following a similar procedure for (4.31), we obtain

$$L_s \frac{di_{sd}}{dt} = L_s\omega(t)i_{sq} + v_d - v_{sd}, \quad (4.90)$$

$$L_s \frac{di_{sq}}{dt} = -L_s\omega(t)i_{sd} + v_q - v_{sq}. \quad (4.91)$$

Equations (4.87)–(4.91) constitute a *dq*-frame model for the circuit of Figure 4.14.

**EXAMPLE 4.9** *dq*-Frame Model of a Second-Order Three-Phase System

Assume that the dynamics of a balanced three-phase system are described by the following space-phasor equation:

$$\frac{d^2}{dt^2} \vec{y} = \vec{u}. \quad (4.92)$$

Equation (4.108) can be further simplified to

$$\begin{bmatrix} \lambda_d \\ \lambda_q \end{bmatrix} = \begin{bmatrix} L_d & 0 \\ 0 & L_q \end{bmatrix} \begin{bmatrix} i_d \\ i_q \end{bmatrix} + \begin{bmatrix} \lambda_m \\ 0 \end{bmatrix}. \quad (4.110)$$

Similarly (4.104) can be rewritten as

$$\frac{d}{dt} \left\{ \mathbf{R}^{-1} \begin{bmatrix} \lambda_d \\ \lambda_q \end{bmatrix} \right\} = \begin{bmatrix} -R_s & 0 \\ 0 & -R_s \end{bmatrix} \mathbf{R}^{-1} \begin{bmatrix} i_d \\ i_q \end{bmatrix} + \mathbf{R}^{-1} \begin{bmatrix} v_{sd} \\ v_{sq} \end{bmatrix}, \quad (4.111)$$

which can be rearranged as

$$\mathbf{R}^{-1} \frac{d}{dt} \begin{bmatrix} \lambda_d \\ \lambda_q \end{bmatrix} + \frac{d\mathbf{R}^{-1}}{dt} \begin{bmatrix} \lambda_d \\ \lambda_q \end{bmatrix} = \begin{bmatrix} -R_s & 0 \\ 0 & -R_s \end{bmatrix} \mathbf{R}^{-1} \begin{bmatrix} i_d \\ i_q \end{bmatrix} + \mathbf{R}^{-1} \begin{bmatrix} v_{sd} \\ v_{sq} \end{bmatrix}. \quad (4.112)$$

Premultiplying both sides of (4.112) by  $\mathbf{R}$  and rearranging the resultant, we deduce

$$\begin{aligned} \frac{d}{dt} \begin{bmatrix} \lambda_d \\ \lambda_q \end{bmatrix} &= -\mathbf{R} \frac{d\mathbf{R}^{-1}}{dt} \begin{bmatrix} \lambda_d \\ \lambda_q \end{bmatrix} + \mathbf{R} \begin{bmatrix} -R_s & 0 \\ 0 & -R_s \end{bmatrix} \mathbf{R}^{-1} \begin{bmatrix} i_d \\ i_q \end{bmatrix} + \begin{bmatrix} v_{sd} \\ v_{sq} \end{bmatrix} \\ &= -\left( \mathbf{R} \frac{d\mathbf{R}^{-1}}{d\theta_r} \right) \left( \frac{d\theta_r}{dt} \right) \begin{bmatrix} \lambda_d \\ \lambda_q \end{bmatrix} + \mathbf{R} \begin{bmatrix} -R_s & 0 \\ 0 & -R_s \end{bmatrix} \mathbf{R}^{-1} \begin{bmatrix} i_d \\ i_q \end{bmatrix} + \begin{bmatrix} v_{sd} \\ v_{sq} \end{bmatrix}. \end{aligned} \quad (4.113)$$

Substituting for  $\mathbf{R}^{-1}$  and  $\mathbf{R}$  in (4.113), one concludes

$$\frac{d}{dt} \begin{bmatrix} \lambda_d \\ \lambda_q \end{bmatrix} = \begin{bmatrix} 0 & \omega_r \\ -\omega_r & 0 \end{bmatrix} \begin{bmatrix} \lambda_d \\ \lambda_q \end{bmatrix} + \begin{bmatrix} -R_s & 0 \\ 0 & -R_s \end{bmatrix} \begin{bmatrix} i_d \\ i_q \end{bmatrix} + \begin{bmatrix} v_{sd} \\ v_{sq} \end{bmatrix}, \quad (4.114)$$

where

$$\frac{d\theta_r}{dt} = \omega_r. \quad (4.115)$$

To derive an expression for the machine torque, the principle of power balance can be used. Based on (4.83), the power delivered to the machine stator is expressed in *dq*-frame as

$$P_e = \frac{3}{2} \begin{bmatrix} i_d \\ i_q \end{bmatrix}^T \begin{bmatrix} v_{sd} \\ v_{sq} \end{bmatrix}. \quad (4.116)$$

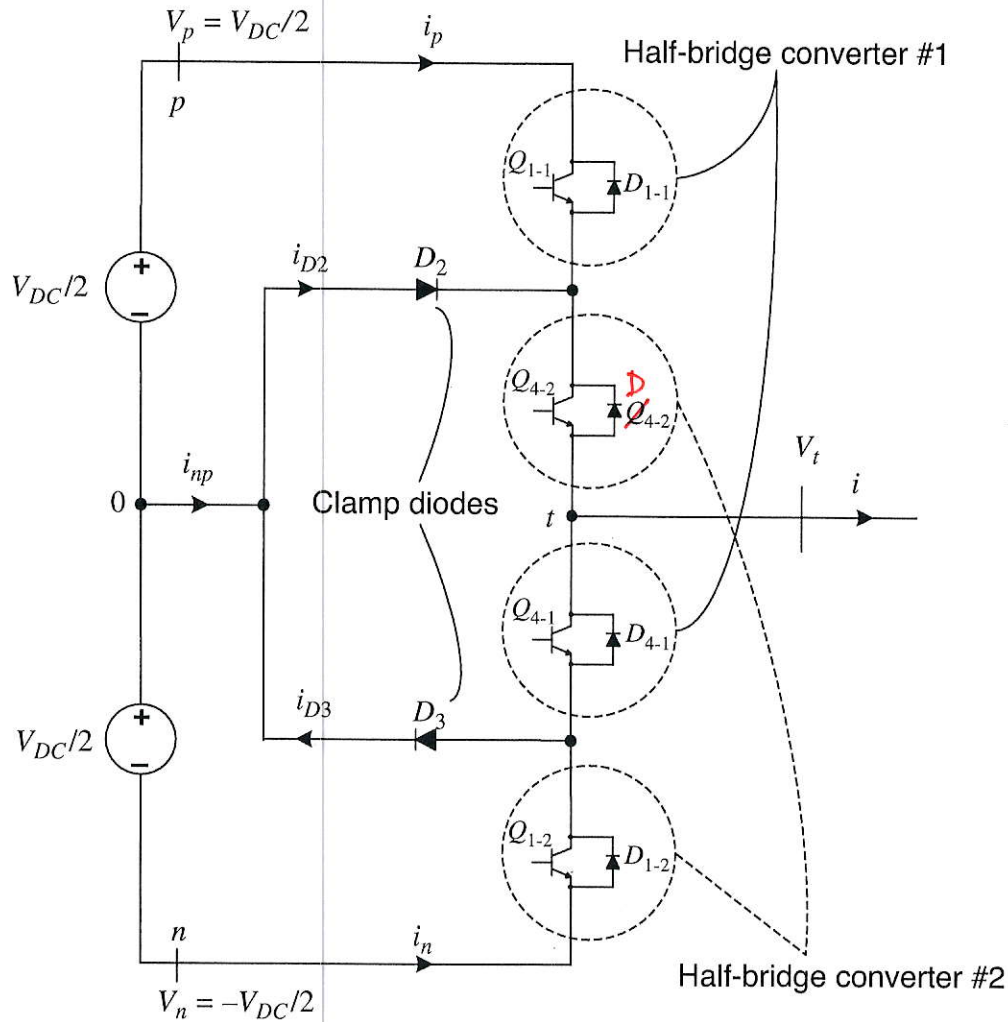


FIGURE 6.1 Circuit diagram of the three-level half-bridge NPC.

configuration shown in Figure 6.2(a). Thus, when  $s_{1-1} = 1$  and  $s_{4-1} = 0$ ,  $Q_{1-1}$  conducts if  $i$  is positive, whereas if  $i$  is negative  $D_{1-1}$  conducts. Consequently, for  $s_{1-1} = 1$  and  $s_{4-1} = 0$ ,  $V_t = V_{DC}/2$ , regardless of the polarity of  $i$ . On the other hand, for  $s_{1-1} = 0$  and  $s_{4-1} = 1$ , if  $i$  is positive,  $D_2$  conducts, whereas if  $i$  is negative,  $Q_{4-1}$  and  $D_3$  conduct. Hence, for  $s_{1-1} = 0$  and  $s_{4-1} = 1$ ,  $V_t = 0$ , irrespective of the polarity of  $i$ . This analysis indicates that when  $s_{1-2} \equiv 0$  and  $s_{4-2} \equiv 1$ , depending on switching states of  $Q_{1-1}$  and  $Q_{4-1}$ , the instantaneous AC-side terminal voltage is either  $V_{DC}/2$  or zero. However, one can control the (positive) average of  $V_t$  by controlling the duty ratios of  $s_{1-1}$  and  $s_{4-1}$  based on a pulse-width modulation (PWM) switching strategy.

### 6.2.2 Generating Negative AC-Side Voltages

To generate a negative voltage at the converter AC-side terminal  $t$ , let  $s_{1-1} \equiv 0$  (or equivalently  $s_{4-1} \equiv 1$ ). Figure 6.2(b) shows the corresponding circuit configuration.

This inequality indicates that the amplitude of the midpoint current can be as high as 76% of the amplitude of the converter AC-side current, corresponding to the scenario where the three-level NPC primarily exchanges reactive power with the AC-side system, for example, when utilized as a static compensator (STATCOM). However, even if the converter operates at (nearly) unity power factor, the amplitude of the midpoint current is not less than 51% of that of the converter AC-side current. Therefore, the DC-side voltage sources must accommodate a relatively large third-harmonic midpoint current, and this can be regarded as a disadvantage of the three-level NPC, as compared to its two-level VSC counterpart. The following example further highlights these conclusions.

51%

### EXAMPLE 6.1 Midpoint Current of Three-Level NPC

Consider the three-level NPC of Figure 6.6 that is interfaced with a three-phase voltage source via three series  $RL$  branches. Figure 6.8(a)–(c), respectively, illustrate the waveforms of the converter AC-side current and fundamental harmonic of the AC-side voltage, the switched waveform of the midpoint current, and the filtered waveform of the midpoint current.

Until  $t = 1.5$  s, the converter fundamental voltage and AC-side current are in phase (unity power factor) (Fig. 6.8(a)) and 710 kW flows out of the converter AC-side terminals. At  $t = 1.5$  s, the converter fundamental voltage is phase

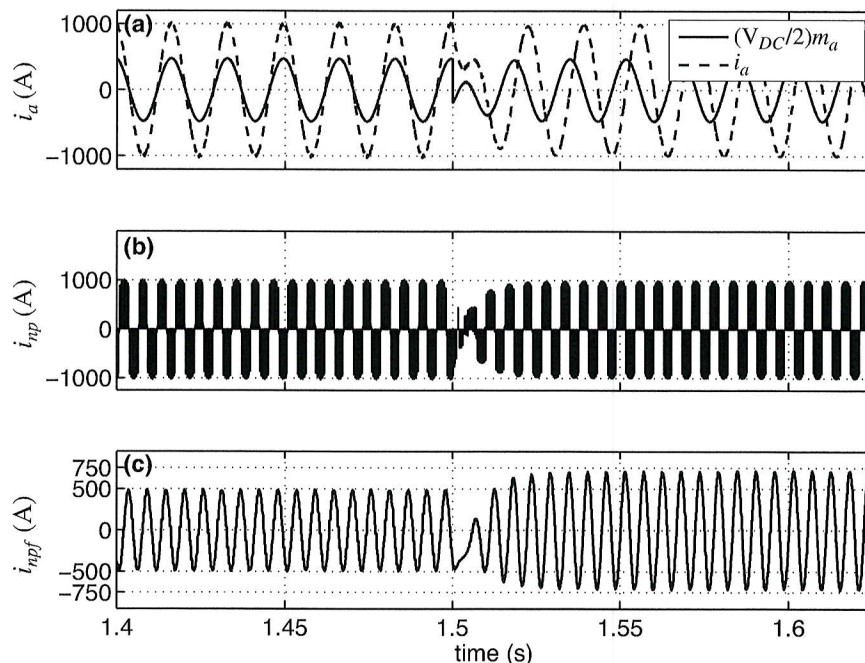


**FIGURE 6.8** Midpoint current of the three-level NPC under unity and zero power-factor conditions; Example 6.1.

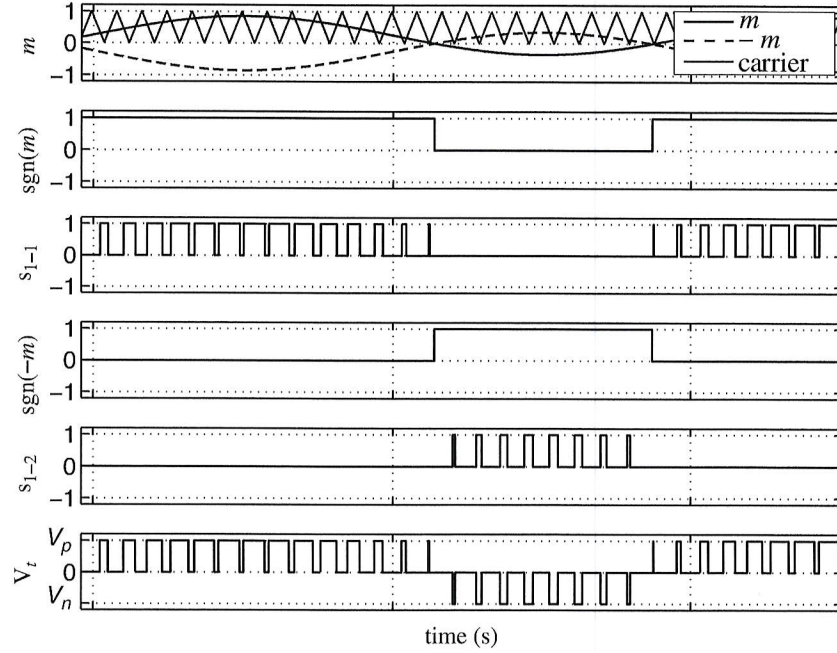


**FIGURE 6.13** Switching functions and AC-side terminal voltage of the three-level half-bridge NPC when the sinusoidal modulating signal is supplemented by a DC offset.

where

$$f_a(t) = m_a(t)i_a(t) [\text{sgn}(m_a) - \text{sgn}(-m_a)], \quad (6.50)$$

$$f_b(t) = m_b(t)i_b(t) [\text{sgn}(m_b) - \text{sgn}(-m_b)], \quad (6.51)$$

$$f_c(t) = m_c(t)i_c(t) [\text{sgn}(m_c) - \text{sgn}(-m_c)]. \quad (6.52)$$

To calculate  $f_a(t) + f_b(t) + f_c(t)$ , we note that based on (6.46)–(6.48),  $m_a(t)$ ,  $m_b(t)$ , and  $m_b(t)$  are identical in form but phase shifted with respect to each other by  $-2\pi/3$ . Therefore, since  $i_{abc}(t)$  is a balanced three-phase waveform,  $f_a(t)$ ,  $f_b(t)$ , and  $f_c(t)$  are also identical in form but phase shifted by  $-2\pi/3$ . Consequently,  $f_a(t) + f_b(t) + f_c(t)$  is three times  $f_a(t)$  with respect to DC and triple- $n$  harmonic components, and zero otherwise. Thus,

$$i_{np0}(t) = -3f_{a0}(t), \quad (6.53)$$

where the subscript 0 denotes the DC component of the corresponding variable. Substituting for  $i_a(t)$  and  $m_a(t)$  in (6.50), respectively, from (6.35) and (6.46), we

$$\begin{aligned}
 f_{a0} &= \frac{m_0 \hat{i}}{2\pi} \left( \int_0^{\pi/2} \cos(\theta - \gamma) d\theta - \int_{\pi/2}^{3\pi/2} \cos(\theta - \gamma) d\theta + \int_{3\pi/2}^{2\pi} \cos(\theta - \gamma) d\theta \right) \\
 &\quad + \frac{\hat{m}\hat{i}}{4\pi} \cos \gamma \left( \int_0^{\pi/2} d\theta - \int_{\pi/2}^{3\pi/2} d\theta + \int_{3\pi/2}^{2\pi} d\theta \right) \\
 &\quad + \frac{\hat{m}\hat{i}}{4\pi} \left( \int_0^{\pi/2} \cos(2\theta - \gamma) d\theta - \int_{\pi/2}^{3\pi/2} \cos(2\theta - \gamma) d\theta + \int_{3\pi/2}^{2\pi} \cos(2\theta - \gamma) d\theta \right) \\
 &= \frac{2\hat{i} \cos \gamma}{\pi} m_0. \tag{6.57}
 \end{aligned}$$

Substituting for  $f_{a0}$  from (6.57) in (6.53), one concludes

$$i_{np0}(t) = -\frac{6\hat{i} \cos \gamma}{\pi} m_0(t). \tag{6.58}$$

Equation (6.58) suggests that the DC component of  $i_{np}$  can be controlled by  $m_0$ . Based on (6.58), the control transfer function is linear, but with a variable gain. The gain is zero if either the three-level NPC AC-side current is small or the converter operates at zero power factor. However, the gain is the largest if the three-level NPC operates at its rated capacity and unity power factor.

To equalize the DC components of the two DC-side voltages, a closed-loop scheme compares them and controls  $m_0$  [61, 65]. Figure 6.15 shows a circuit model of the DC-side voltages and the midpoint current in which partial DC-side voltages are denoted by  $V_1$  and  $V_2$ . Figure 6.15 indicates that  $i_{np}$  has two components: a third-harmonic component,  $i_{np3}$ , and a DC component,  $i_{np0}$ , which are formulated by (6.45) and (6.58), respectively. As an approximation, we assume that the capacitors are identical, each with a capacitance of  $2C$ .

If  $V_{DC}$ , that is, the net DC-side voltage, has no third-harmonic component, it can be replaced by a short circuit. Thus, the circuit of Figure 6.15 is simplified to the equivalent circuit of Figure 6.16(a), for the third-harmonic component. Based on Figure 6.16(a) and since the capacitors are identical,  $i_{np3}$  is equally divided between the two capacitors, and  $i_1 = -i_2 = i_{np3}/2$ , where  $i_{np3}$  is expressed by (6.45). Hence, in a steady state, the third-order harmonic components of  $V_1$  and  $V_2$  are given by

$$\langle V_1 \rangle_3 = \hat{V}_{r3} \sin(3\omega t + \zeta) \tag{6.59}$$

$$\langle V_2 \rangle_3 = -\hat{V}_{r3} \sin(3\omega t + \zeta), \tag{6.60}$$

where  $\omega = d\varepsilon/dt$  and  $\zeta = \pi - \tan^{-1}(1.5 \tan \gamma)$ , and the peak voltage ripple  $\hat{V}_{r3}$  is

$$\hat{V}_{r3} = \frac{\hat{m}\hat{i}}{15\pi C\omega} \sqrt{9 - 5 \cos^2 \gamma}. \tag{6.61}$$

and

$$\begin{aligned} i_a(t) &= \hat{i} \cos(\theta - \phi), \\ i_b(t) &= \hat{i} \cos\left(\theta - \phi - \frac{2\pi}{3}\right), \\ i_c(t) &= \hat{i} \cos\left(\theta - \phi - \frac{4\pi}{3}\right), \end{aligned} \quad (7.18)$$

where  $\theta = \omega_0 t + \theta_0$ ;  $\delta$  and  $-\phi$  are, respectively, the phase shifts of  $V_{tabc}$  and  $i_{abc}$  with respect to  $V_{sabc}$ . Under steady-state conditions,  $\phi$  is the power-factor angle of the VSC system, in the conventional phasor analysis sense. Based on (4.2), the space phasors corresponding to  $V_{sabc}$  and  $i_{abc}$  are

$$\vec{V}_s(t) = \hat{V}_s e^{j\theta}, \quad (7.19)$$

$$\vec{i}(t) = \hat{i} e^{-j\phi} e^{j\theta}. \quad (7.20)$$

Substituting for  $\vec{V}_s$  and  $\vec{i}$  in (4.38) and (4.40), one obtains the real and reactive power delivered to the AC system as

$$P_s = \frac{3}{2} \hat{i} \hat{V}_s \cos \phi, \quad (7.21)$$

$$Q_s = \frac{3}{2} \hat{i} \hat{V}_s \sin \phi. \quad (7.22)$$

Equations (7.21) and (7.22) are rearranged as

$$\hat{i} \cos \phi = P_s / \left( \frac{3}{2} \hat{V}_s \right), \quad (7.23)$$

$$\hat{i} \sin \phi = Q_s / \left( \frac{3}{2} \hat{V}_s \right). \quad (7.24)$$

Based on (4.46), the  $\alpha$ -axis components of  $V_{sabc}$ ,  $V_{tabc}$ , and  $i_{abc}$  are

$$V_{s\alpha} = \hat{V}_s \cos \theta, \quad (7.25)$$

$$V_{t\alpha} = \hat{V}_t \cos(\theta + \delta) = \hat{V}_t \cos \delta \cos \theta - \hat{V}_t \sin \delta \sin \theta, \quad (7.26)$$

$$i_\alpha = \hat{i} \cos(\theta - \phi) = \hat{i} \cos \phi \cos \theta + \hat{i} \sin \phi \sin \theta. \quad (7.27)$$

Substituting for  $\hat{i} \cos \phi$  and  $\hat{i} \sin \phi$  in (7.27), from (7.23) and (7.24), substituting for  $V_{s\alpha}$ ,  $V_{t\alpha}$ , and  $i_\alpha$  in (7.12), from (7.25), (7.26), and (7.27), and assuming  $(R + r_{on}) \approx 0$ ,

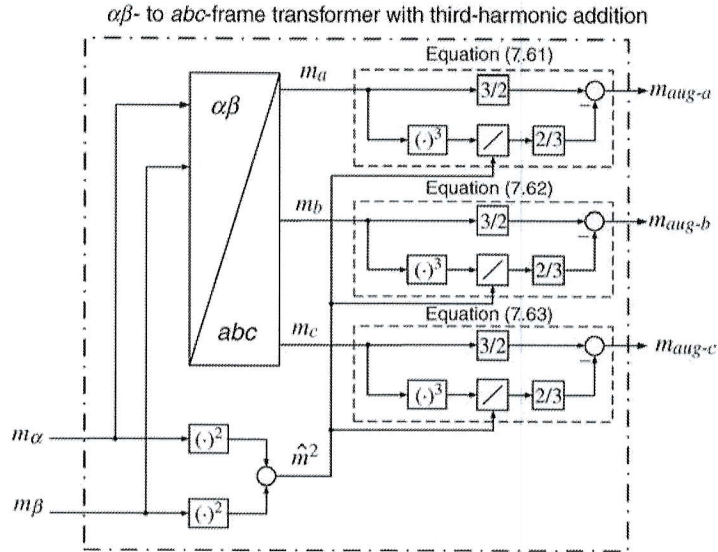


FIGURE 7.11 Block diagram of the  $\alpha\beta$ - to  $abc$ -frame signal transformer used for third-harmonic injected PWM.

As Figure 7.12 illustrates, for a VSC employing the third-harmonic injected PWM, each component of  $m_{aug-abc}$  is limited to  $\pm 1$ . This is equivalent to  $|m_{abc}| < 1$  for a VSC that employs the conventional PWM strategy. Thus, based on the third-harmonic

1.15

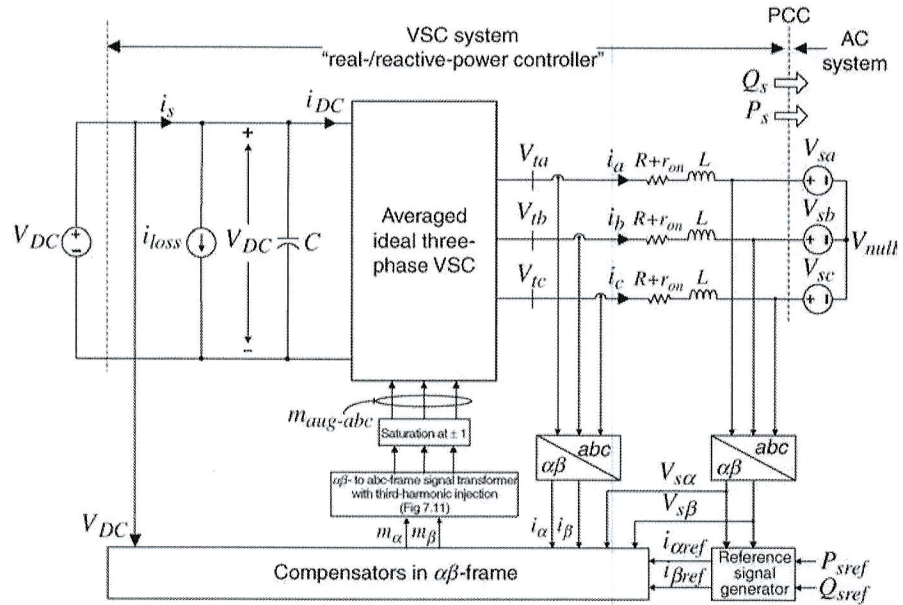


FIGURE 7.12 Schematic diagram of the real-/reactive-power controller adopting the third-harmonic injected PWM.

be a proper transfer function.<sup>4</sup> The following example demonstrates the design procedure.

**EXAMPLE 7.3 Real-/Reactive-Power Controller Based on the Three-level NPC**

Consider the VSC system of Figure 7.12 that utilizes the three-level NPC of Figure 7.14 and adopts the third-harmonic injected PWM strategy. The system parameters and controllers are the same as those in Example 7.1, except that  $2C = 19250 \mu\text{F}$ ,  $r_{on} = 0.44 \text{ m}\Omega$ , and  $V_{DC} = 1.25 \text{ kV}$ . The rated power of the system of Figure 7.12 is  $P_s = 1.0 \text{ MW}$ . Based on  $\hat{m} = 2\hat{V}_t/V_{DC}$  and assuming  $\hat{V}_t \approx \hat{V}_s = 0.391 \text{ kV}$ , we obtain  $\hat{m} \approx 0.63$ . Thus, the plant transfer function, in the closed-loop system of Figure 7.16, is

$$G(s) = \left( \frac{4}{\pi C V_{DC} \hat{m}} \right) \frac{1}{s} = \frac{168}{s} \quad [(\text{kA})^{-1}].$$

Let  $F(s)$  be

$$F(s) = \frac{s^2 + (3\omega_0)^2}{(s + 3\omega_0)^2} = \frac{s^2 + 1131^2}{s^2 + 2262s + 1131^2},$$

where  $\omega_0 = 377 \text{ rad/s}$ . Then, (i) the third-harmonic component of  $V_1 - V_2$  is suppressed, (ii)  $F(s)$  has a unity DC gain, and (iii) the loop gain continues to roll off for frequencies beyond  $3\omega_0$ . If a pure gain is considered for the compensator, that is,  $K(s) = k$ , and  $|P_s| = 1 \text{ MW}$ , then the loop gain is

$$\ell(s) = K(s)G(s)F(s)|P_s| = (168k) \frac{s^2 + 1131^2}{s(s^2 + 2262s + 1131^2)}.$$

For  $\omega \leq \omega_0/10$ , the phase of  $\ell(j\omega)$  is almost constant at  $-90^\circ$ , corresponding to a phase margin of  $90^\circ$ . For  $\omega$  larger than  $\omega_0/10$ , due to the double real pole at  $\omega = \omega_0$ , the phase drops with a slope of approximately  $-90^\circ/\text{dec}$ . Thus, if we need a phase margin of, for example,  $70^\circ$ , we should select the loop gain crossover frequency, that is,  $\omega_c$ , to be about  $1.93$  decade larger than  $\omega_0/10$ , that is,  $\omega_c = 218 \text{ rad/s}$ . Substituting for  $\omega_c = 218 \text{ rad/s}$  in equation  $|\ell(j\omega_c)| = 1$ , we find  $k = 1.40 \text{ (kV)}^{-1}$ , for which the exact phase margin is  $68^\circ$ , and the closed-loop poles are located at  $s = -1910 \text{ rad/s}$  and  $s = -294 \pm j267 \text{ rad/s}$ . Figure 7.17 shows the frequency responses of the loop gain and closed-loop transfer function. It is observed that the bandwidth of the closed-loop system is about  $\omega_b = 400 \text{ rad/s}$ . The closed-loop transfer function is  $G_{cl}(s) = |P_s|K(s)G(s)/(1 + \ell(s))$ .

*Handwritten notes:*  $3\omega_0$  (circled),  $3\omega_0$  (circled),  $3\omega_0$  (circled),  $0.288$ ,  $64^\circ$ ,  $70^\circ$  (circled),  $3\omega_0$ ,  $220$ ,  $218$  (circled),  $220$ .

<sup>4</sup>By definition, a proper transfer function is one whose denominator has a degree equal to or higher than that of its numerator.

Equation (7.85) can be solved for  $P_t$  as

$$P_t = P_s + \frac{3}{2}(R + r_{on})\widehat{i}^2 + \frac{3L}{2} \operatorname{Re} \left\{ \frac{d\vec{i}}{dt} \vec{i}^* \right\}. \quad (7.86)$$

As shown in Example ~~4.5~~<sup>4.6</sup>, the term  $\frac{3L}{2} \operatorname{Re} \left\{ \frac{d\vec{i}}{dt} \vec{i}^* \right\}$  is the instantaneous power absorbed by the three-phase inductor bank  $L$  (see (4.41)) and  $\frac{3}{2}(R + r_{on})\widehat{i}^2$  is the power dissipated by the resistance of the three-phase inductor.

Practically,  $(R + r_{on})$  is a small resistance and its associated power is negligible compared to  $P_t$  and  $P_s$ . However, the power absorbed by the three-phase inductor can be significant during transients. The reason is that, since in a high-power VSC the switching frequency is limited by power loss considerations,  $L$  must be adequately large to suppress the switching harmonics. Furthermore, since the  $\alpha\beta$ -frame current controllers are fast,  $\vec{i}$  can undergo rapid phase and amplitude changes, during the real-/reactive-power command tracking process. Substituting for  $\vec{i} = i_\alpha + ji_\beta$  in (4.41), we obtain

$$\frac{3L}{2} \operatorname{Re} \left\{ \frac{d\vec{i}}{dt} \vec{i}^* \right\} = \frac{3L}{4} \frac{d}{dt} (i_\alpha^2 + i_\beta^2) = \frac{3L}{4} \frac{d\widehat{i}^2}{dt}. \quad (7.87)$$

Based on (4.40), we deduce

$$P_s + jQ_s = \frac{3}{2} \vec{V}_s \vec{i}^*. \quad (7.88)$$

Applying the complex-conjugate operator to (7.88) and multiplying the resultant by (7.88), we deduce

$$P_s^2 + Q_s^2 = \frac{9}{4} \widehat{V}_s^2 \widehat{i}^2. \quad (7.89)$$

Substituting for  $\widehat{i}^2$  from (7.89) in (7.87), and assuming that  $\widehat{V}_s$  is constant, we obtain

$$\frac{3L}{2} \operatorname{Re} \left\{ \frac{d\vec{i}}{dt} \vec{i}^* \right\} = \left( \frac{L}{3\widehat{V}_s^2} \right) \frac{dP_s^2}{dt} + \left( \frac{L}{3\widehat{V}_s^2} \right) \frac{dQ_s^2}{dt}. \quad (7.90)$$

Thus, (7.86) can be rewritten as

$$P_t \approx P_s + \left( \frac{2L}{3\widehat{V}_s^2} \right) P_s \frac{dP_s}{dt} + \left( \frac{2L}{3\widehat{V}_s^2} \right) Q_s \frac{dQ_s}{dt}. \quad (7.91)$$

Substituting for  $P_t$  from (7.91) in (7.83), we have

$$\begin{aligned} \frac{dV_{DC}^2}{dt} = & \frac{2}{C}P_{ext} - \frac{2}{C}P_{loss} - \frac{2}{C} \left[ P_s + \left( \frac{2LP_s}{3\hat{V}_s^2} \right) \frac{dP_s}{dt} \right] \\ & - \frac{2}{C} \left[ \left( \frac{2LQ_s}{3\hat{V}_s^2} \right) \frac{dQ_s}{dt} \right]. \end{aligned} \quad (7.92)$$

Equation (7.92) describes dynamics of  $V_{DC}^2$ . Based on (7.92),  $V_{DC}^2$  is the output,  $P_s$  is the control input, and  $P_{ext}$ ,  $P_{loss}$ , and  $Q_s$  are the disturbance inputs. Thus, to control  $V_{DC}^2$ , one can form the control scheme shown in Figure 7.22, which consists of an inner control loop nested inside an outer loop. The outer loop compares  $V_{DC}^2$  with the reference  $V_{DCref}^2$ , processes the error by a compensator, and delivers  $P_{sref}$  to the inner control loop. The inner control loop is the real-power controller detailed in Section 7.3, which regulates  $P_s$  at its reference,  $P_{sref}$ .

In the system of Figure 7.22,  $Q_s$  can be independently controlled. If the command  $Q_{sref}$  is set to zero, the VSC system operates at unity power factor. However,  $Q_{sref}$  may be set to a positive or a negative value, depending on the required level of the reactive-power exchange with the AC system; this is the operational strategy of a STATCOM. If the AC system has a significant equivalent impedance, the voltage at the PCC is subject to variations depending on the load changes and/or level of the real-power exchange. In this case, the PCC voltage can be regulated by controlling  $Q_s$ , via a closed-loop system that monitors the PCC voltage and determines  $Q_{sref}$ . The STATCOM mode of operation and the AC voltage regulation strategy through reactive-power control are discussed in Chapter 11.

Figure 7.22 illustrates that an estimate of  $P_{ext}$  can be added as a feed-forward signal to the output of the compensator  $K_v(s)$ . Thus, a change in  $P_{ext}$  is rapidly reflected in  $P_{sref}$ , and its impact on  $V_{DC}^2$  is mitigated. Such an estimate of  $P_{ext}$  is available in many applications. For example, if the power source connected to the VSC system of Figure 7.22 is another VSC system that controls an electric machine,  $P_{ext}$  is approximately equal to the product of the machine torque and speed, ignoring the power losses of the machine and VSC. Figure 7.22 also shows that the compensator output, augmented by the measure of  $P_{ext}$ , is passed through a saturation block before the real-power controller. This ensures that the VSC is protected from overcurrent conditions in case the DC-bus voltage is subjected to a significant deviation from its reference value, or in case there is a large excursion in  $P_{ext}(t)$ .

In the VSC system of Figure 7.22, the compensator  $K_v(s)$  is designed according to (7.92), which indicates that  $P_{ext}$  and  $P_{loss}$  impact  $V_{DC}^2$  under both transient and steady-state conditions. The impact of  $P_{ext}$  is, to a great extent, mitigated by the feed-forward compensation. However,  $P_{loss}$  cannot be measured or estimated with certainty to be compensated by the feed-forward compensation. Therefore, to eliminate the steady-state error of  $V_{DC}^2$  due to  $P_{loss}$ ,  $K_v(s)$  must include an integral term. Since the control plant also includes an integral term, to ensure stability and an adequate phase margin,  $K_v(s)$  must also include a zero.

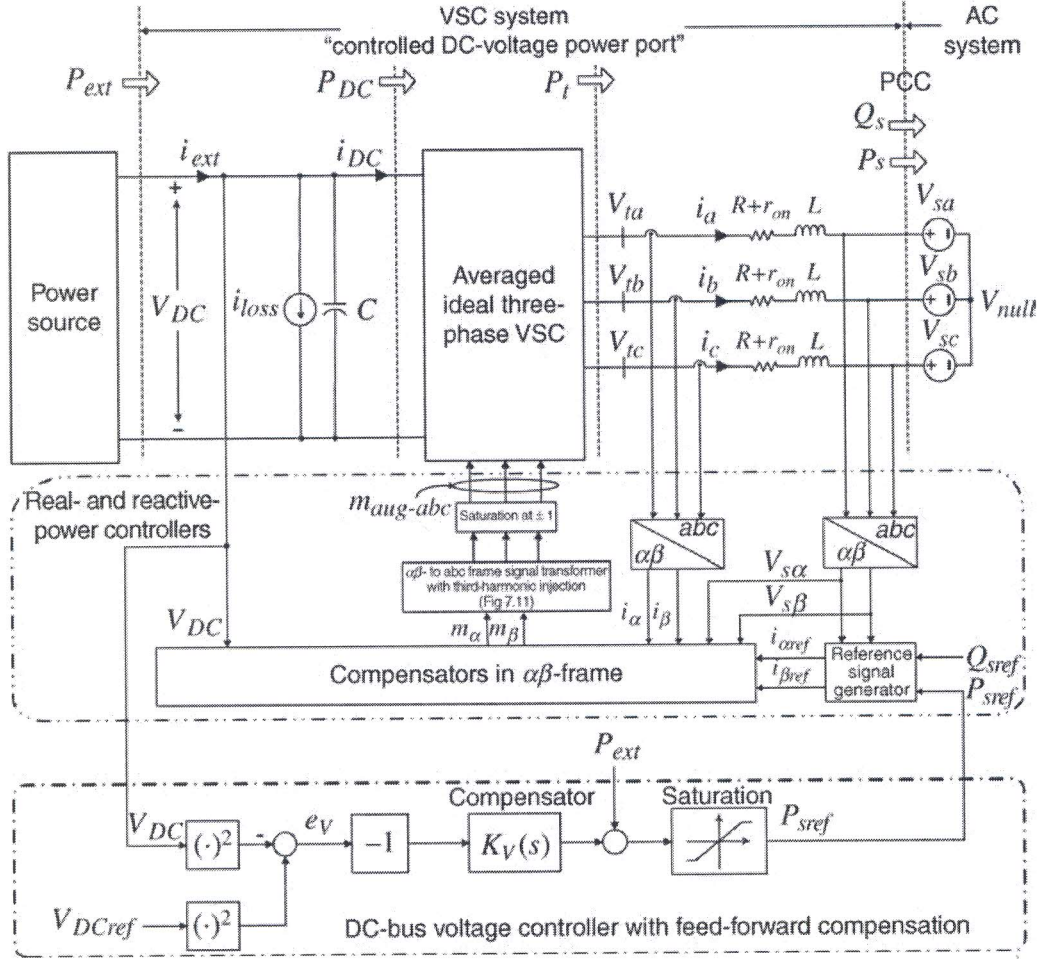


**FIGURE 7.22** Schematic diagram of the controlled DC-voltage power port with DC-bus voltage regulator.

Due to the presence of terms  $P_s \frac{dP_s}{dt}$  and  $Q_s \frac{dQ_s}{dt}$ , the control plant described by (7.92) is nonlinear. Thus, to design  $K_V(s)$ , we first linearize (7.92) about a steady-state operating point, which is computed by replacing all the derivatives in (7.92) by zero. Thus,

$$P_{s0} = P_{ext0} - P_{loss} \approx P_{ext0}, \quad (7.93)$$

and (7.92) is linearized as

$$\begin{aligned} \frac{d\tilde{V}_{DC}^2}{dt} &= \frac{2}{C} \tilde{P}_{ext} - \frac{2}{C} \left[ \tilde{P}_s + \left( \frac{2LP_{s0}}{3\hat{V}_s^2} \right) \frac{d\tilde{P}_s}{dt} \right] \\ &\quad - \frac{2}{C} \left[ \left( \frac{2LQ_{s0}}{3\hat{V}_s^2} \right) \frac{d\tilde{Q}_s}{dt} \right], \end{aligned} \quad (7.94)$$

operating points. The three operating points correspond to  $\tau = 0.43$  ms,  $\tau = 0$ , and  $\tau = -0.43$  ms, respectively.

$-180^\circ$

Figure 7.24 illustrates that the magnitude plot is similar for all three operating points and  $|\ell(j700)| = 1$ . Moreover, the closed-loop system is stable for the positive rated real power, with a phase margin of about  $18^\circ$ . However, the loop is unstable under the zero-power and the negative rated power operating points, as  $\angle\ell(j700)$  is correspondingly equal to  $180^\circ$  and  $-197^\circ$ . Based on parameters of this specific example, the closed-loop system is stable, although poorly, for the positive rated power; however, it becomes unstable as the power becomes increasingly negative [72].

To design the compensator, let us consider the worst-case scenario that corresponds to the negative rated real-power operating point, for which  $\angle\ell(j700) \approx -197^\circ$ . Thus, if a phase margin of, for example,  $45^\circ$  is required,  $62^\circ$  must be added to  $\angle\ell(j700)$ . This can be achieved by means of a lead filter, as explained in Example 3.6. Let  $H(s)$  be the lead filter

$$H(s) = h \frac{s + (p_1/\alpha)}{s + p_1}, \quad (7.101)$$

where  $p_1$  is the filter pole and  $\alpha > 1$  is a real constant. The maximum phase of the lead filter is

$$\delta_m = \sin^{-1} \left( \frac{\alpha - 1}{\alpha + 1} \right), \quad (7.102)$$

which corresponds to the frequency

$$\omega_m = \frac{p_1}{\sqrt{\alpha}}. \quad (7.103)$$

In our example,  $\delta_m = 62^\circ$  and  $\omega_m = \omega_c = 700$  rad/s. Hence, based on (7.102) and (7.103), we obtain  $\alpha = 16.1$  and  $p_1 = 2808$  rad/s, and (7.101) becomes

$$H(s) = h \frac{s + 174.4}{s + 2808}. \quad (7.104)$$

Solving for  $h$  based on  $|H(j700)| = \omega_c^2$ , one finds  $h = 1,965,666$  s $^{-2}$ . Substituting for  $H(s)$  from (7.104) in (7.98), one concludes

$$K_v(s) = 9459 \frac{s + 174.4}{s(s + 2808)} \quad [\Omega^{-1}]. \quad (7.105)$$

Dashed lines in Figure 7.24 illustrate the Bode plots of the compensated loop gain. Figure 7.24 shows that for all the three operating points, the magnitude of  $\ell(j\omega)$  remains similar to that of the uncompensated loop, and

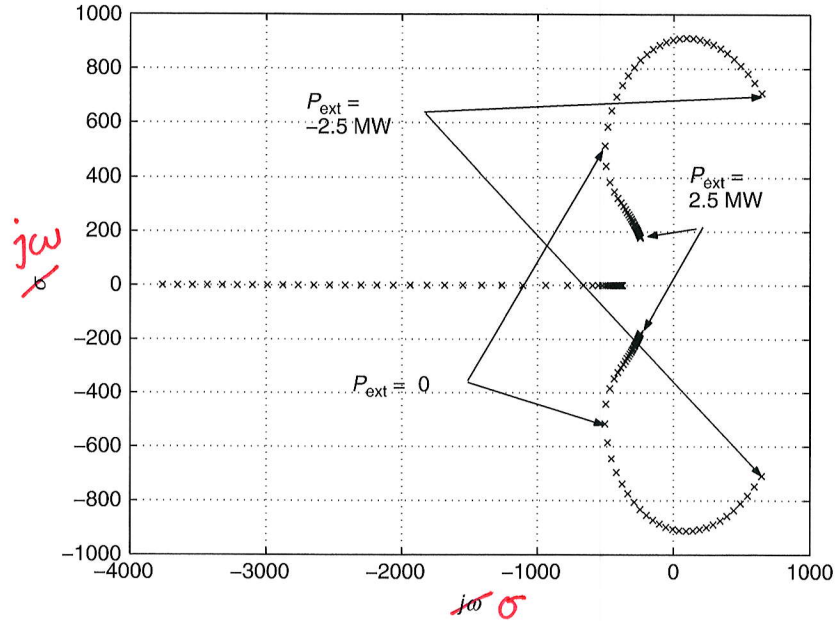


FIGURE 7.28 Root loci of the closed-loop DC-bus voltage controller; Example 7.5.

### EXAMPLE 7.5 Instability in the Rectifying Mode of Operation

Consider the controlled DC-voltage power port of Figure 7.22 with parameters  $L = 200 \mu\text{H}$ ,  $R = 2.38 \text{ m}\Omega$ ,  $r_{on} = 0.88 \text{ m}\Omega$ ,  $V_d = 1.0 \text{ V}$ ,  $V_{DC} = 1250 \text{ V}$ , and  $f_s = 1620 \text{ Hz}$ . The line-to-line rms voltage of the AC system is 480 V and its frequency is 377 rad/s. The  $\alpha$ - and  $\beta$ -axis compensators of the real-/reactive-power controller are

$$K_\alpha(s) = K_\beta(s) = 2516 \left( \frac{s + 16.34}{s^2 + 377^2} \right) \left( \frac{s + 966}{s + 5633} \right) \left( \frac{s + 2}{s + 0.05} \right) \quad [\Omega]. \quad (7.108)$$

Each compensator provides a closed-loop bandwidth of about  $\omega_b = 3820 \text{ rad/s}$  (see Example 3.6 for details) for the corresponding loop. The transfer function of the feed-forward filter is  $G_{ff}(s) = 1/(8 \times 10^{-6}s + 1)$ . In this example, the PWM switching frequency is smaller than that of the VSC system of Example 7.4. Therefore, to achieve low harmonic distortion for the AC-side current, inductances of the interface reactors are larger than those of the VSC system of Example 7.4. However, since the switching frequency is reduced, the VSC system of this example can operate at a relatively higher power level.

We design the DC-bus voltage controller based on the simplified model of (7.107). Thus, the (simplified) plant is an integrator and has the phase  $-90^\circ$  regardless of the operating point. Assuming that a phase margin of  $45^\circ$  is required at a gain crossover frequency of  $\omega_c = 700 \text{ rad/s}$ , following the procedure

# 8 Grid-Imposed Frequency VSC System: Control in $dq$ -Frame

## 8.1 INTRODUCTION

Chapter 5 presented dynamic models for the two-level VSC in  $\alpha\beta$ -frame and  $dq$ -frame and briefly discussed its control based on generic block diagrams of Figures 5.5 and 5.7. Chapter 6 introduced the three-level NPC as an extension of the two-level VSC and established that the dynamic model of the three-level NPC is identical to that of the two-level VSC, except that the three-level NPC requires a DC-side voltage equalizing system to maintain DC-side capacitor voltages, each at half the net DC-side voltage. Thus, Chapter 6 presented a unified model for the three-level NPC and the two-level VSC (Fig. 6.18 and 6.19). Chapter 7 introduced a class of VSC systems referred to as *grid-imposed frequency VSC systems*. On the basis of the unified model of Chapter 6, Chapter 7 presented  $\alpha\beta$ -frame models and controls for two members of the family of the grid-imposed frequency VSC systems, namely, the *real/reactive-power controller* and the *controlled DC-voltage power port*. In parallel with Chapter 7, this chapter presents  $dq$ -frame models and controls for the real/reactive-power controller and the controlled DC-voltage power port.

As discussed in Chapter 7, compared to the  $abc$ -frame control, the  $\alpha\beta$ -frame control of a grid-imposed frequency VSC system reduces the number of plants to be controlled from three to two. Moreover, instantaneous decoupled control of the real and reactive power, exchanged between the VSC system and the AC system, is possible in  $\alpha\beta$ -frame. However, the control variables, that is, feedback signals, feed-forward signals, and control signals are sinusoidal functions of time. It is shown in this chapter that the  $dq$ -frame control of a grid-imposed VSC system features all merits of the  $\alpha\beta$ -frame control, in addition to the advantage that the control variables are DC quantities in the steady state. This feature ~~X~~ remarkably facilitates the compensator design, especially in variable-frequency scenarios.

To achieve zero steady-state error in the  $\alpha\beta$ -frame control, the bandwidth of the closed-loop system must be adequately larger than the AC system frequency; alternatively, the compensators can include complex-conjugate pairs of poles at the AC system frequency and other frequencies of interest, to increase the loop gain. In the  $dq$ -frame control, however, zero steady-state error is readily achieved by including

### 8.3.4 Phase-Locked Loop (PLL)

Substituting for  $\vec{V}_s(t)$  from (8.4) in (8.1), we deduce

$$V_{sd} = \hat{V}_s \cos(\omega_0 t + \theta_0 - \rho), \quad (8.18)$$

$$V_{sq} = \hat{V}_s \sin(\omega_0 t + \theta_0 - \rho). \quad (8.19)$$

Thus, (8.11)–(8.13) can be rewritten as

$$L \frac{di_d}{dt} = L\omega(t)i_q - (R + r_{on})i_d + V_{td} - V_{sd}, \quad (8.20)$$

$$L \frac{di_q}{dt} = -L\omega(t)i_d - (R + r_{on})i_q + V_{tq} - V_{sq}, \quad (8.21)$$

$$\frac{d\rho}{dt} = \omega(t). \quad (8.22)$$

Based on (8.19),  $\rho(t) = \omega_0 t + \theta_0$  corresponds to  $V_{sq} = 0$ . Therefore, we devise a mechanism to regulate  $V_{sq}$  at zero. This can be achieved based on the following feedback law:

$$\omega(t) = H(p)V_{sq}(t), \quad (8.23)$$

where  $H(p)$  is a linear transfer function (compensator) and  $p = d(\cdot)/dt$  is a differentiation operator. Substituting for  $V_{sq}$  from (8.19) in (8.23), and substituting for  $\omega$  from (8.23) in (8.22), we deduce

$$\frac{d\rho}{dt} = H(p)\hat{V}_s \sin(\omega_0 t + \theta_0 - \rho). \quad (8.24)$$

Equation (8.24) describes a nonlinear dynamic system, which is referred to as PLL [49], [78–80]. The function of the PLL is to regulate  $\rho$  at  $\omega_0 t + \theta_0$ . However, in view of its nonlinear characteristic, the PLL can exhibit unsatisfactory behavior under certain conditions. For example, if the PLL starts from an initial condition corresponding to  $\rho(0) = 0$  and  $\omega(0) = 0$ , then the term  $\hat{V}_s H(p) \sin(\omega_0 t + \theta_0 - \rho)$  in (8.24) is a sinusoidal function of time with frequency  $\omega_0$ . Then, if  $H(s)$  has a low-pass frequency response, the right-hand side of (8.24) and also  $d\rho/dt$  exhibit small sinusoidal perturbations about zero, the PLL falls in a limit cycle, and  $\rho$  does not track  $\omega_0 t + \theta_0$ . To prevent the limit cycle from taking place, the control law can be modified as

$$\omega(t) = H(p)V_{sq}(t), \quad \omega(0) = \omega_0 \quad \text{and} \quad \omega_{min} \leq \omega \leq \omega_{max}, \quad (8.25)$$

where  $\omega(t)$  has the initial value  $\omega(0) = \omega_0$  and is limited to the lower and upper limits of, respectively,  $\omega_{min}$  and  $\omega_{max}$ .  $\omega_{min}$  and  $\omega_{max}$  are selected to be close to  $\omega_0$  and thus to define a narrow range of variations for  $\omega(t)$ . On the other hand, the range of

each to provide  $45^\circ$  at 200 rad/s. Thus,

$$F(s) = \left( \frac{s + (p/\alpha)}{s + p} \right) \left( \frac{s + (p/\alpha)}{s + p} \right), \quad (8.33)$$

where

$$p = \omega_c \sqrt{\alpha} \quad (8.34)$$

$$\alpha = \frac{1 + \sin \delta_m}{1 - \sin \delta_m}, \quad (8.35)$$

and  $\delta_m$  is the phase of each lead compensator at  $\omega_c$ . If  $\delta_m = 45^\circ$ , based on (8.33)–(8.35), we calculate  $F(s)$  as

$$F(s) = \left( \frac{s + 83}{s + 482} \right)^2. \quad (8.36)$$

Substituting for  $F(s)$  from (8.36) in (8.32), we deduce

$$\ell(s) = \frac{h (s^2 + 568,516) (s^2 + 166s + 6889)}{s^2 (s^2 + 1508s + 568,516) (s^2 + 964s + 232,324)}. \quad (8.37)$$

It then follows from  $|\ell(j200)| = 1$  and  $\widehat{V}_{sn} = 391$  V that  $h = 2.68 \times 10^5$ . Therefore,  $h/\widehat{V}_{sn} = 685.42$  and the final compensator is

$$H(s) = \frac{685.42 (s^2 + 568,516) (s^2 + 166s + 6889)}{s (s^2 + 1508s + 568,516) (s^2 + 964s + 232,324)} \quad [(\text{rad/s})/\text{V}]. \quad (8.38)$$

Figure 8.6 depicts the frequency response of  $\ell(j\omega)$  based on the compensator of (8.38). It is observed that  $|\ell(j\omega)|$  drops with the slope of  $-40$  dB/dec, for  $\omega \ll \omega_c = 200$ . However, around  $\omega_c$  the slope of  $|\ell(j\omega)|$  reduces to about  $-20$  dB/dec and  $\angle\ell(j\omega)$  rises to about  $-120^\circ$  at  $\omega = \omega_c$ , corresponding to a phase margin of  $60^\circ$ . Figure 8.6 also illustrates that  $|\ell(j\omega)|$  continues to drop with a slope of  $-40$  dB/dec for  $\omega > \omega_c$ . This characteristic is desired as the AC components of  $V_{sq}$  due to the harmonic distortion of  $V_{sabc}$  are attenuated. In particular, at  $\omega = 6\omega_0$ ,  $|\ell(j\omega)|$  is about  $-30$  dB.

Figure 8.7 illustrates the start-up transient of the PLL. Figure 8.7 shows that, initially, from  $t = 0$  to  $t = 0.07$  s, the compensator output is saturated at  $\omega_{min} = 2\pi \times 55$  rad/s and, therefore,  $V_{sd}$  and  $V_{sq}$  vary with time. At about  $t = 0.07$  s,  $V_{sq}$  crosses zero and intends to become negative. Thus,  $H(s)$  increases  $\omega$  to regulate  $V_{sq}$  at zero. Figure 8.7 indicates that  $V_{sq}$  is regulated at zero within 0.15 s. It should be noted that if  $\omega_{min}$  is selected closer to  $\omega_0$ , the start-up transient period becomes shorter. However,  $\omega_{min}$  cannot be selected too close to  $\omega_0$  since the PLL would not be able to quickly react to other types of disturbance.

becomes positive thereafter

0.02

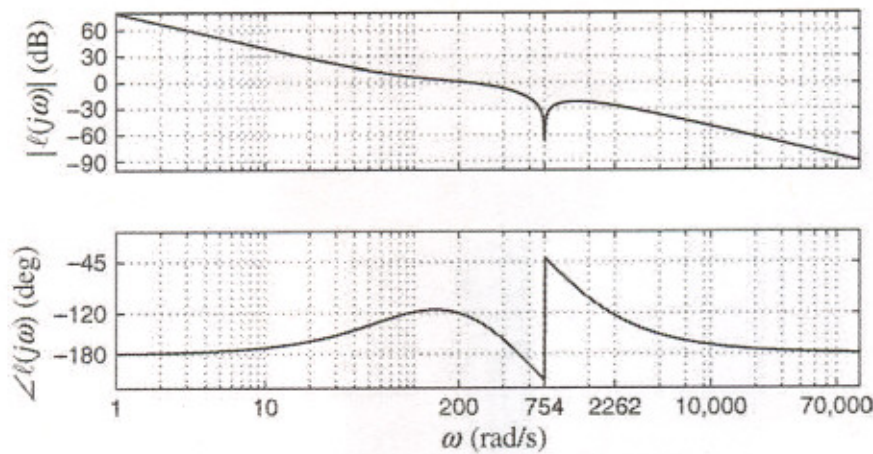


FIGURE 8.6 Open-loop frequency response of the PLL of Example 8.1.

Figure 8.8 illustrates the dynamic response of the PLL to a sudden imbalance in  $V_{sabc}$ . Initially, the PLL is in a steady state. At  $t = 0.05$  s, the AC system voltage  $V_{sabc}$  becomes unbalanced such that  $\hat{V}_s$  and  $k_1$  undergo step changes, respectively, from 391 to 260 V and from zero to 0.5, and at  $t = 0.15$  s,  $V_{sabc}$

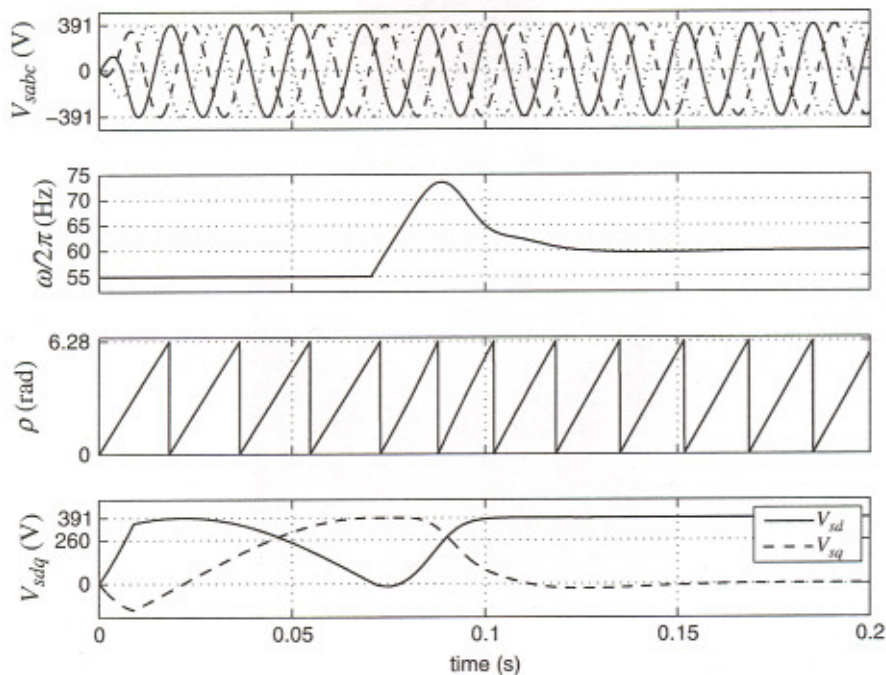


FIGURE 8.7 Start-up response of the PLL of Example 8.1.

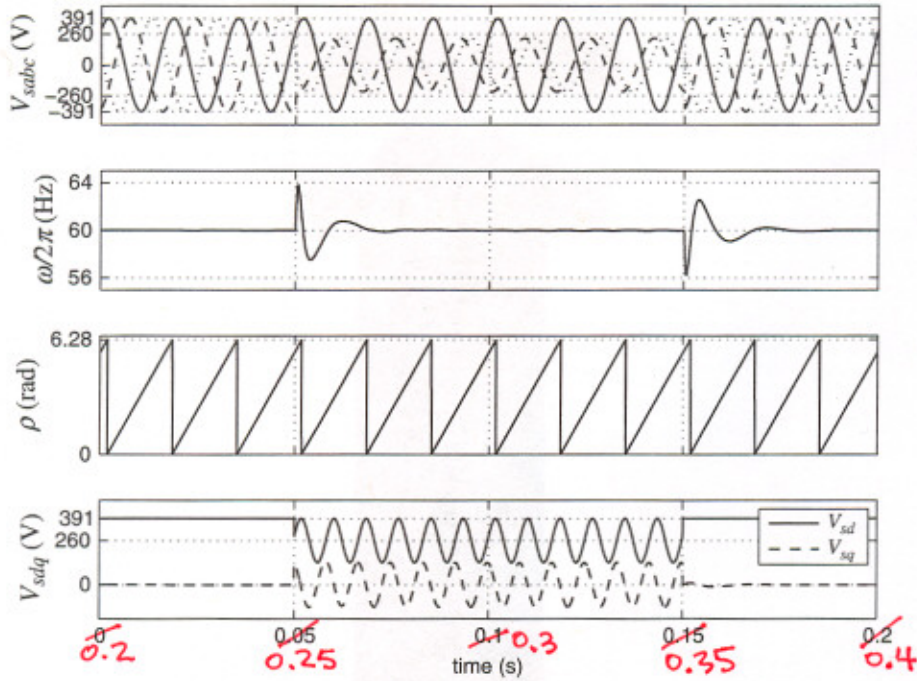


FIGURE 8.8 Response of the PLL of Example 8.1 to a sudden AC system voltage imbalance.

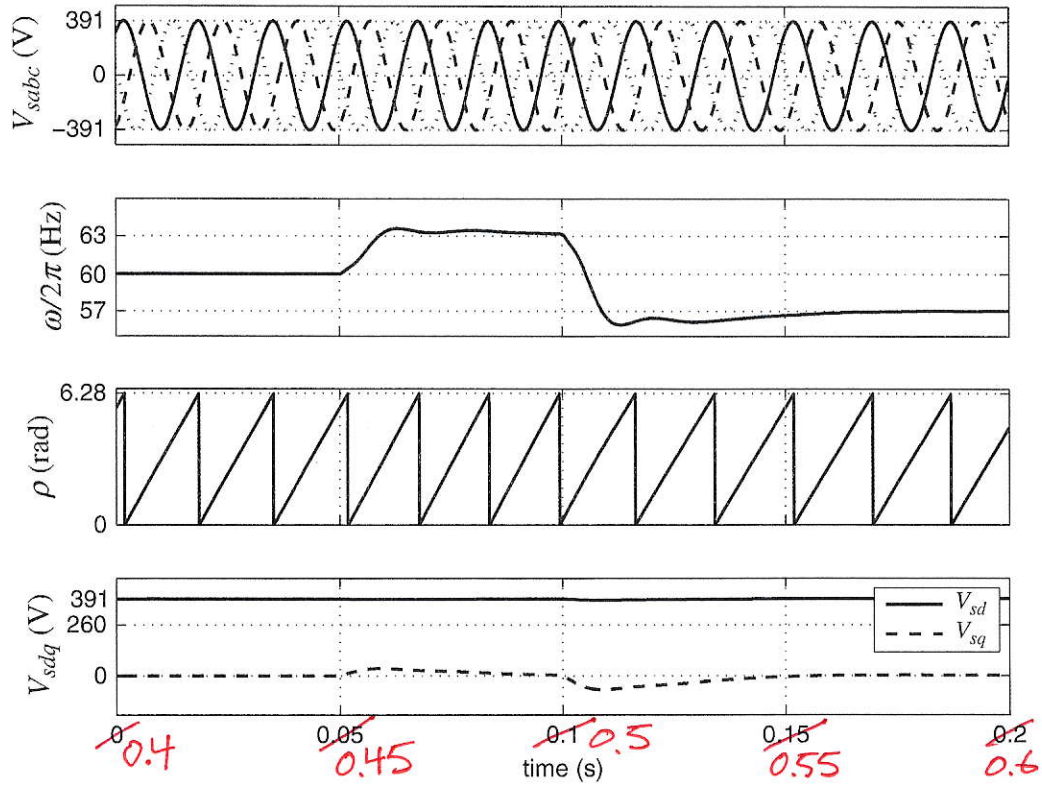
reverts to its balanced predisturbance condition. In response to the voltage imbalance,  $H(s)$  transiently changes  $\omega$ , as Figure 8.8 shows, to maintain the DC component of  $V_{sq}$  at zero. Figure 8.8 also shows that  $V_{sq}$  (and  $V_{sd}$ ) includes a 120-Hz sinusoidal ripple due to the negative-sequence component of  $V_{sabc}$ . The ripple is, however, suppressed by  $H(s)$ , and  $\omega$  and  $\rho$  remain free of distortion.

Figure 8.9 depicts the dynamic response of the PLL to two stepwise changes in  $\omega_0$ , the first one from  $2\pi \times 60 = 377$  rad/s to  $2\pi \times 63 = 396$  rad/s at  $t = 0.05$  s, and the other from 396 rad/s to  $2\pi \times 57 = 358$  rad/s at  $t = 0.1$  s. As Figure 8.9 shows,  $V_{sq}$  is rapidly regulated at zero and  $\omega$  tracks the changes.

Equation (8.31) denotes that  $H(s)$  is normalized such that the constant gain of the loop gain  $h$  is independent of  $\hat{V}_{sn}$ . Thus, in subsequent chapters when we need a PLL, we will employ the compensator of (8.38), but modify its constant gain, that is,  $h/\hat{V}_{sn}$ , according to  $\hat{V}_{sn}$  for the specific problem in hand, based on  $h = 2.68 \times 10^5$ .

#### 8.4 CURRENT-MODE CONTROL OF REAL-/REACTIVE-POWER CONTROLLER

With reference to the real-/reactive-power controller of Figure 8.3, based on (4.83) and (4.84), the real and reactive power delivered to the AC system at



**FIGURE 8.9** Response of the PLL of Example 8.1 to a sudden AC system frequency change.

the PCC are

$$P_s(t) = \frac{3}{2} [V_{sd}(t)i_d(t) + V_{sq}(t)i_q(t)], \quad (8.39)$$

$$Q_s(t) = \frac{3}{2} [-V_{sd}(t)i_q(t) + V_{sq}(t)i_d(t)], \quad (8.40)$$

where  $V_{sd}$  and  $V_{sq}$  are the AC system  $dq$ -frame voltage components and cannot be controlled by the VSC system. As described in Section 8.3.4, if the PLL is in a steady state,  $V_{sq} = 0$  and (8.39) and (8.40) can be rewritten as

$$P_s(t) = \frac{3}{2} V_{sd}(t)i_d(t), \quad (8.41)$$

$$Q_s(t) = -\frac{3}{2} V_{sd}(t)i_q(t). \quad (8.42)$$

Therefore, based on (8.41) and (8.42),  $P_s(t)$  and  $Q_s(t)$  can be controlled by  $i_d$  and  $i_q$ , respectively. Let us introduce

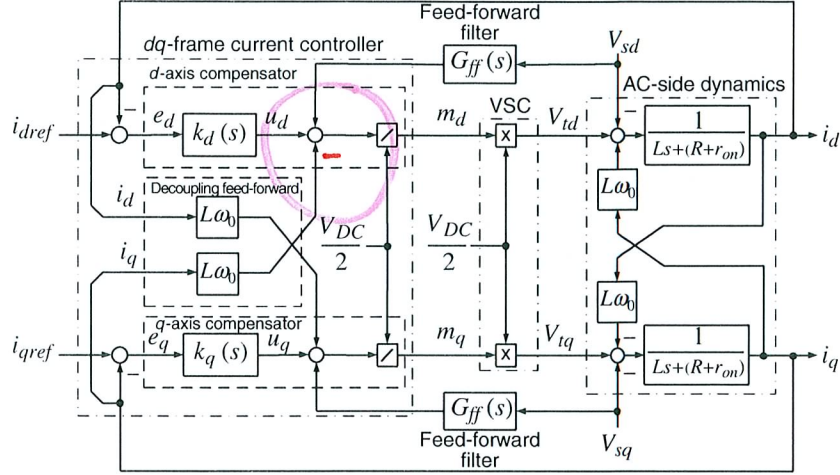


FIGURE 8.10 Control block diagram of a current-controlled VSC system.

$V_{iq}$  from the resultant in (8.45) and (8.46), we deduce

$$L \frac{di_d}{dt} = -(R + r_{on})i_d + u_d, \quad (8.51)$$

$$L \frac{di_q}{dt} = -(R + r_{on})i_q + u_q. \quad (8.52)$$

Equations (8.51) and (8.52) describe two decoupled, first-order, linear systems. Based on (8.51) and (8.52),  $i_d$  and  $i_q$  can be controlled by  $u_d$  and  $u_q$ , respectively. Figure 8.10 shows a block representation of the  $d$ - and  $q$ -axis current controllers of the VSC system in which  $u_d$  and  $u_q$  are the outputs of two corresponding compensators. The  $d$ -axis compensator processes  $e_d = i_{dref} - i_d$  and provides  $u_d$ . Then, based on (8.49),  $u_d$  contributes to  $m_d$ . Similarly, the  $q$ -axis compensator processes  $e_q = i_{qref} - i_q$  and provides  $u_q$  that, based on (8.50), contributes to  $m_q$ . The VSC then amplifies  $m_d$  and  $m_q$  by a factor of  $V_{DC}/2$  and generates  $V_{id}$  and  $V_{iq}$  that, in turn, control  $i_d$  and  $i_q$  based on (8.45) and (8.46). On the basis of the above-mentioned control process, one can sketch the simplified control block diagram of Figure 8.11, which is equivalent to the control system of Figure 8.10. It should be noted that in the control system of Figure 8.10, all the control, feed-forward, and feedback signals are DC quantities in the steady state.

Figure 8.11 indicates that the control plants in both  $d$ - and  $q$ -axis current-control loops are identical. Therefore, the corresponding compensators can also be identical. Consider the  $d$ -axis control loop. Unlike the  $\alpha\beta$ -frame control where the compensators are fairly difficult to optimize and typically are of high dynamic orders,  $k_d(s)$  can be a simple proportional-integral (PI) compensator to enable tracking of a DC reference

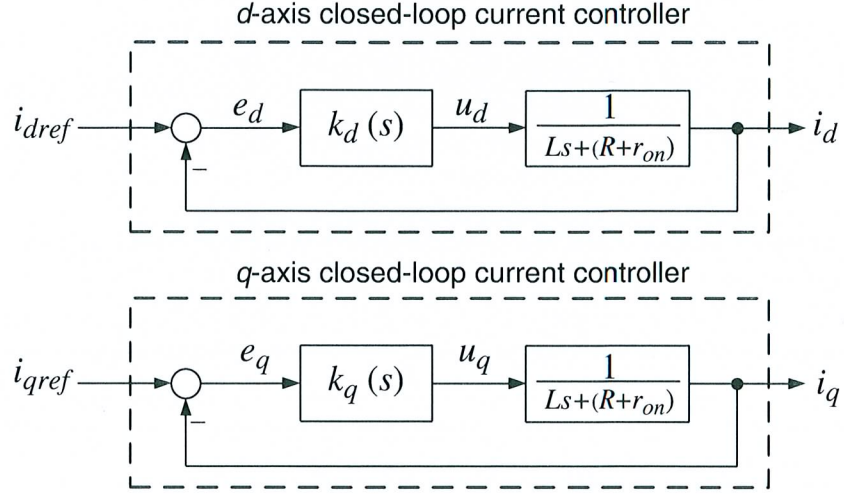


FIGURE 8.11 Simplified block diagram of the current-controlled VSC system of Figure 8.10.

command. Let

$$k_d(s) = \frac{k_p s + k_i}{s}, \quad (8.53)$$

where  $k_p$  and  $k_i$  are proportional and integral gains, respectively. Thus, the loop gain is

$$\ell(s) = \left( \frac{k_p}{Ls} \right) \frac{s + k_i/k_p}{s + (R + r_{on})/L}. \quad (8.54)$$

It is noted that due to the plant pole at  $s = -(R + r_{on})/L$ , which is fairly close to the origin, the magnitude and the phase of the loop gain start to drop from a relatively low frequency. Thus, the plant pole is first canceled by the compensator zero  $s = -k_i/k_p$ , and the loop gain assumes the form  $\ell(s) = k_p/(Ls)$ . Then, the closed-loop transfer function, that is,  $\ell(s)/(1 + \ell(s))$ , becomes

$$\frac{I_q(s)}{I_{qref}(s)} = \frac{I_d(s)}{I_{dref}(s)} = G_i(s) = \frac{1}{\tau_i s + 1}, \quad (8.55)$$

if

$$k_p = L/\tau_i, \quad (8.56)$$

$$k_i = (R + r_{on})/\tau_i. \quad (8.57)$$

where  $\tau_i$  is the time constant of the resultant closed-loop system.

#### 8.4.2 Selection of DC-Bus Voltage Level

As discussed in Sections 7.3.4, 7.3.5, and 7.3.6, the DC-bus voltage of the real-/reactive-power controller of Figure 8.3 must satisfy the following criteria:

$$V_{DC} \geq 2\widehat{V}_t, \quad \text{PWM}, \quad (8.58)$$

$$V_{DC} \geq 1.74\widehat{V}_t, \quad \text{PWM with third-harmonic injection}. \quad (8.59)$$

Thus, one must properly evaluate  $\widehat{V}_t$  under the worst-case operating condition. Since the VSC system controls  $P_s$  and  $Q_s$ ,  $\widehat{V}_t$  should also be expressed in terms of  $P_s$  and  $Q_s$ . Based on (8.45) and (8.46), and under the assumptions that  $V_{sq} = 0$  and  $(R + r_{on}) \approx 0$ , we deduce

$$V_{id} = L \frac{di_d}{dt} - L\omega_0 i_q + V_{sd}, \quad (8.60)$$

$$V_{iq} = L \frac{di_q}{dt} + L\omega_0 i_d. \quad (8.61)$$

Substituting for  $i_d$  and  $i_q$  from (8.41) and (8.42) in (8.60) and (8.61), and assuming that  $V_{sd}$  is constant, we obtain

$$V_{id} = \left( \frac{2L}{3V_{sd}} \right) \frac{dP_s}{dt} + \left( \frac{2L\omega_0}{3V_{sd}} \right) Q_s + V_{sd}, \quad (8.62)$$

$$V_{iq} = - \left( \frac{2L}{3V_{sd}} \right) \frac{dQ_s}{dt} + \left( \frac{2L\omega_0}{3V_{sd}} \right) P_s. \quad (8.63)$$

Based on (4.77), the amplitude of the AC-side terminal voltage is

$$\widehat{V}_t = \sqrt{V_{id}^2 + V_{iq}^2}. \quad (8.64)$$

Furthermore, the amplitude of the modulating signal is

$$\widehat{V}_t = \widehat{m} \frac{V_{DC}}{2}. \quad (8.65)$$

As discussed in Section 7.3.6, if the conventional PWM is employed,  $\widehat{m}$  can assume a value up to unity, whereas with the PWM with third-harmonic injection,  $\widehat{m}$  can be as large as 1.15.

To calculate the maximum of  $\widehat{V}_t$ , consider the following worst-case scenario. Initially, the system is under a steady-state condition, that is,  $P_s = P_{sref} = P_{s0}$  and  $Q_s = Q_{sref} = Q_{s0}$ . At  $t = t_0$ ,  $P_{sref}$  and  $Q_{sref}$  are subjected to step changes from  $P_{s0}$  to  $P_{s0} + \Delta P_s$ , and  $Q_{s0}$  to  $Q_{s0} + \Delta Q_s$ , respectively. As discussed in Section 8.4.1,

As (8.41) and (8.42) indicate,  $P_s$  and  $Q_s$  are directly related to  $I_d$  and  $I_q$ , respectively (assuming that  $V_{sd}$  is constant). Thus, based on (8.55),

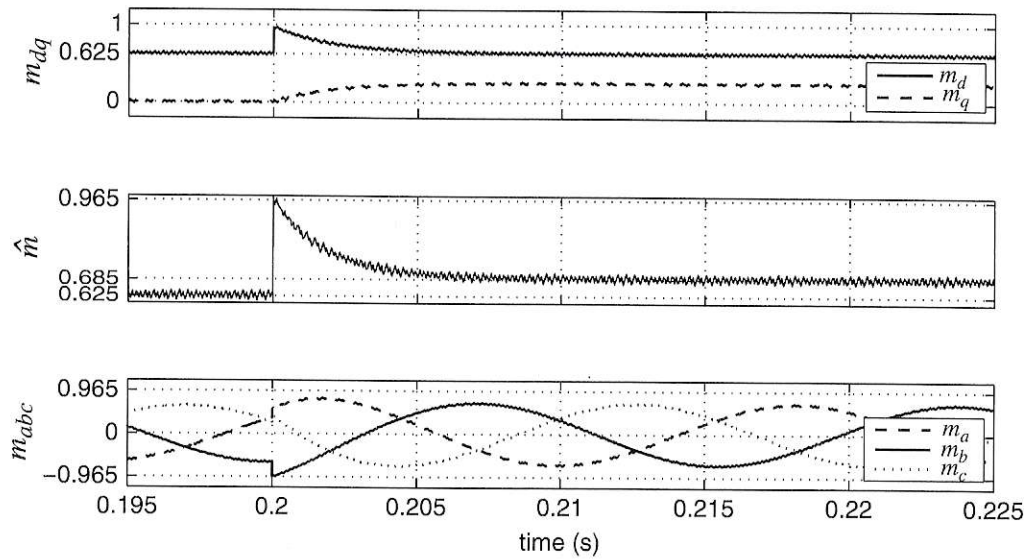


**FIGURE 8.14** Steady-state and dynamic responses of the modulating signals to step change in  $P_{sref}$ ; Example 8.3.

PWM is employed,  $V_{DC}$  must be larger than 1.208 kV (equation (8.58)) to avoid overmodulation. However, if the third-harmonic injected PWM is employed,  $V_{DC}$  can be lowered to about 1.050 kV (equation (8.59)). For the VSC system of Example 8.2,  $V_{DC} = 1.250$  kV was selected since the conventional PWM was employed.

8.3

Figure 8.14 illustrates the waveforms of  $m_d$ ,  $m_q$ , and  $\hat{m}$  for the VSC system of Example 8.2. Figure 8.14 illustrates that at  $t_0 = 0.2$  s,  $\hat{m}$  jumps to 0.965, corresponding to  $\hat{V}_t = 0.604$  kV. Figure 8.14 also indicates that in this specific example, the instant when the disturbance takes place coincides with the instant when  $m_b(t)$  reaches its negative peak; this corresponds to the worst-case scenario. However, since the DC-bus voltage is adequately large, neither  $\hat{m}$  nor  $|m_b(t_0)|$  exceed unity, and the VSC does not experience overmodulation.

### 8.4.3 AC-Side Equivalent Circuit

Traditionally, balanced three-phase linear circuits have been analyzed based on their corresponding phasor diagrams and single-phase equivalent circuits. In the conventional phasor analysis, which is restricted to steady-state conditions, the voltages and currents are represented by phasors, and the passive elements are represented by impedances. This section first presents a space-phasor diagram, analogous to the conventional phasor diagram, for the AC side of the real-/reactive-power controller of Figure 8.3. Then, the relationships between the magnitude/phase-angle of an AC-side variable and the  $d$ -/ $q$ -axis components of the variable are identified. It is also demonstrated that, under steady-state conditions, the space-phasor differential equations of the real-/reactive-power controller become equivalent to the algebraic

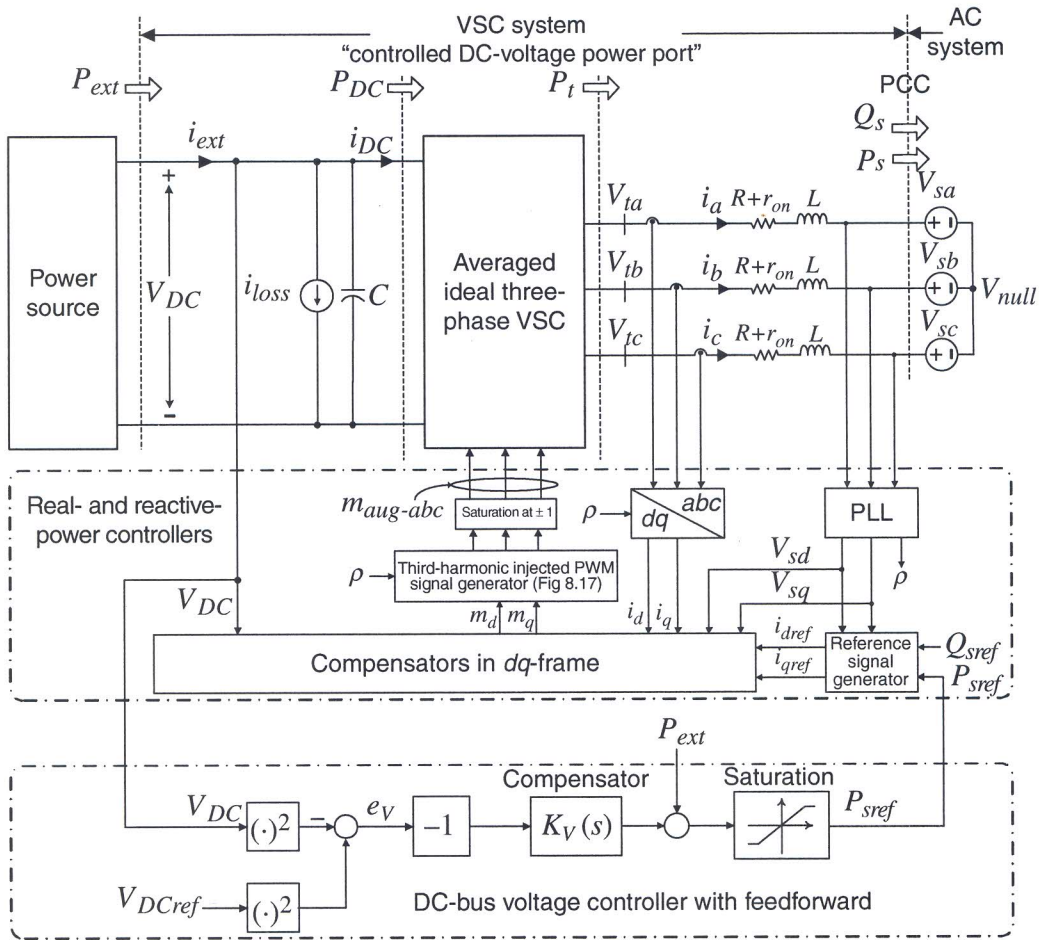


FIGURE 8.21 Schematic diagram of the controlled DC-voltage power-port.

### 8.6.1 Model of Controlled DC-Voltage Power Port

The main control requirement of the controlled DC-voltage power port of Figure 8.21 is to regulate the DC-bus voltage,  $V_{DC}$ . Equivalently, as discussed in Section 7.5.1, we choose to regulate  $V_{DC}^2$  rather than  $V_{DC}$ . Based on (7.92), dynamics of  $V_{DC}^2$  are described by

$$\frac{dV_{DC}^2}{dt} = \frac{2}{C} P_{ext} - \frac{2}{C} P_{loss} - \frac{2}{C} \left[ P_s + \left( \frac{2LP_s}{3V_{sd}^2} \right) \frac{dP_s}{dt} \right] - \frac{2}{C} \left[ \left( \frac{2LQ_s}{3V_{sd}^2} \right) \frac{dQ_s}{dt} \right], \quad (8.90)$$

where  $\hat{V}_s$  of (7.92) is replaced by  $V_{sd}$ . Based on the unified dynamic model of the two-level VSC and the three-level NPC that was presented in Section 6.7.4, (8.90) is valid for both VSC configurations. Based on (8.90),  $V_{DC}^2$  is the output,  $P_s$  is the

control input, and  $P_{ext}$ ,  $P_{loss}$ , and  $Q_s$  are the disturbance inputs. As shown in Figure 8.21,  $V_{DC}^2$  is compared with  $V_{DCref}^2$ , the error signal is processed by the compensator  $K_v(s)$ , and the command  $P_{sref}$  is issued for the real-power controller. The real-power controller, in turn, regulates  $P_s$  at  $P_{sref}$ , while  $Q_s$  can be independently controlled.  $Q_{sref}$  can be set to a nonzero value if an exchange of reactive power with the AC system is required. In an AC system with a large impedance, the PCC voltage is subject to variations as  $P_s$  changes with time (i.e., due to the changes of  $P_{ext}$ ). In this case, the PCC voltage can be regulated by controlling  $Q_s$  in a closed-loop system that feeds the PCC voltage back and commands  $Q_{sref}$ ; this reactive-power control strategy is discussed in Chapter 11.

To derive the transfer function  $G_p(s) = P_s(s)/P_{sref}(s)$ , we note that

$$I_d(s) = G_i(s)I_{dref}(s), \quad (8.91)$$

where  $G_i(s)$  is given by (8.55). Assuming that  $V_{sd}$  is constant, multiplying both sides of (8.91) by  $(3/2)V_{sd}$ , we obtain

$$P_s(s) = G_i(s)P_{sref}(s). \quad (8.92)$$

Therefore,  $G_p(s) = G_i(s)$  and based on (8.55), we have

$$\frac{P_s(s)}{P_{sref}(s)} = G_p(s) = \frac{1}{\tau_i s + 1}. \quad (8.93)$$

The form of (8.93) is intuitively expected as real power in  $dq$ -frame is proportional to  $i_d$ . The control plant described by (8.90) is nonlinear due to  $P_s \frac{dP_s}{dt}$  and  $Q_s \frac{dQ_s}{dt}$  terms. The linearized plant is provided by (7.94), which is repeated here as (8.94), in which  $\tilde{V}_s$  is substituted by  $V_{sd}$ .

$$\begin{aligned} \frac{d\tilde{V}_{DC}^2}{dt} = & \frac{2}{C}\tilde{P}_{ext} - \frac{2}{C} \left[ \tilde{P}_s + \left( \frac{2LP_{s0}}{3V_{sd}^2} \right) \frac{d\tilde{P}_s}{dt} \right] \\ & - \frac{2}{C} \left[ \left( \frac{2LQ_{s0}}{3V_{sd}^2} \right) \frac{d\tilde{Q}_s}{dt} \right], \end{aligned} \quad (8.94)$$

where superscripts  $\sim$  and 0 represent, respectively, small-signal perturbations and steady-state values of the variables. Applying Laplace transform to (8.94), we deduce the transfer function  $G_v(s) = \tilde{V}_{DC}^2(s)/\tilde{P}_s(s)$  as

$$G_v(s) = \tilde{V}_{DC}^2(s)/\tilde{P}_s(s) = - \left( \frac{2}{C} \right) \frac{\tau s + 1}{s}, \quad (8.95)$$

where  $G_v(s)$  and  $G_p(s)$  are given by (8.95) and (8.97), respectively. To ensure zero steady-state errors,  $K_v(s)$  must include an integral term. Let  $K_v(s)$  be

$$K_v(s) = N(s) \frac{k_0}{s}, \quad (8.99)$$

where  $N(s)$  is a proper transfer function with no zero at  $s = 0$ , and  $k_0$  is a constant gain. Substituting for  $G_v(s)$  and  $K_v(s)$  in (8.98), respectively, from (8.95) and (8.99), we obtain

$$\ell(s) = N(s)k_0 \left( \frac{2}{C} \right) \frac{\tau s + 1}{s^2 (0.001s + 1)}. \quad (8.100)$$

If  $N(s) = 1$ , then  $k_0 = 180$  yields  $|\ell(j200)| = 1$  and

$$\ell(s) = 37423 \frac{\tau s + 1}{s^2 (0.001s + 1)}. \quad (8.101)$$

We refer to (8.101) as the *uncompensated* loop gain.

Figure 8.23 illustrates the magnitude and phase plots of the uncompensated loop gain, for  $P_{ext0} = 2.5$  MW,  $P_{ext0} = 0$ , and  $P_{ext0} = -2.5$  MW. Figure 8.23 shows that the magnitude response of the uncompensated loop gain is similar for all three operating points, and  $|\ell(j200)| = 1$ . However,  $\angle \ell(j200)$  is  $-168^\circ$ ,  $-191^\circ$ , and  $-215^\circ$ , corresponding to  $P_{ext0} = 2.5$ , 0, and  $-2.5$  MW, respectively. Therefore, the closed-loop system is poorly stable for  $P_{ext0} = 2.5$  MW, and unstable for  $P_{ext0} = 0$  and  $P_{ext0} = -2.5$  MW. To ensure a stable closed-loop system for all operating points, we correct  $\angle \ell(j200)$  by letting  $N(s)$  in (8.100) be the lead filter

$$N(s) = n_0 \frac{s + (p/\alpha)}{s + p}, \quad (8.102)$$

where  $p$  is the filter pole,  $\alpha (> 1)$  is a real constant, and  $n_0$  is the filter gain. The maximum phase of the filter is given by

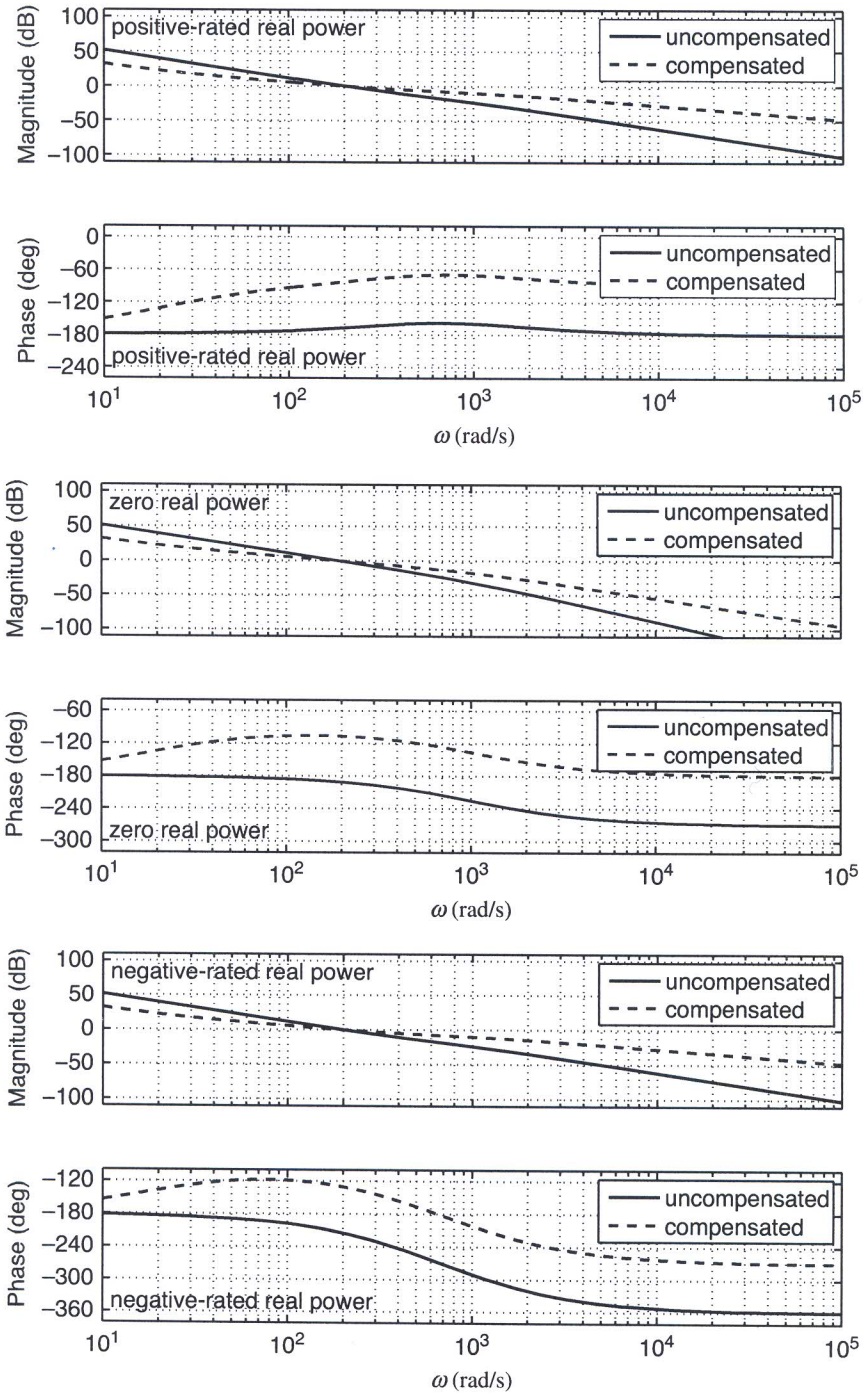
$$\delta_m = \sin^{-1} \left( \frac{\alpha - 1}{\alpha + 1} \right), \quad (8.103)$$

which corresponds to the frequency

$$\omega_m = \frac{p}{\sqrt{\alpha}}. \quad (8.104)$$

Thus, if a phase margin of, for example,  $45^\circ$  is desired for  $P_{ext} = -2.5$  MW, then  $\angle N(j200)$  is required to be  $80^\circ$ . Solving for  $\alpha$ ,  $p$ , and  $n_0$ , with  $\delta_m = 80^\circ$ ,

$$\alpha = 79, \quad p = 79, \quad n_0 = 44$$



The plots of the compensated loop gain are incorrect at high frequencies. Please see the correct plots on the next page.

FIGURE 8.23 Bode plot of the open-loop gain of the DC-bus voltage controller; Example 8.4.

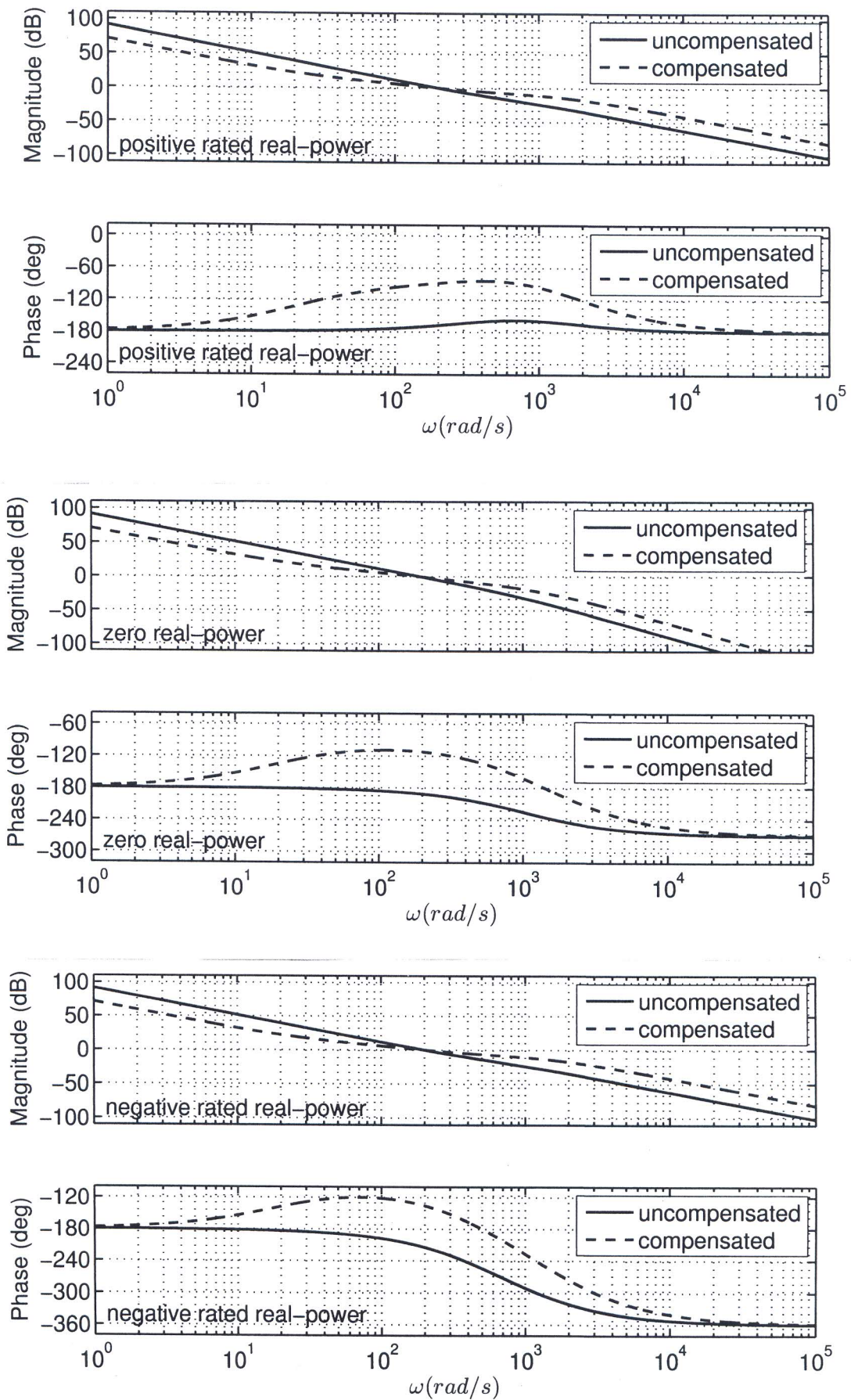


Fig. 8.23 - Correct Bode Plots (Page 240)

$\omega_m = 200$  rad/s, and  $|N(j200)| = 1$ , we obtain

$$N(s) = 10.38 \frac{s + 19}{s + 2077} \quad (8.105)$$

Substituting for  $N(s)$  in (8.99) and (8.100), from (8.105), we obtain

$$\ell(s) = 388455 \left( \frac{s + 19}{s + 2077} \right) \left( \frac{\tau s + 1}{s^2 (0.001s + 1)} \right), \quad (8.106)$$

$$K_v(s) = 1868 \frac{s + 19}{s(s + 2077)} \quad [\Omega^{-1}]. \quad (8.107)$$

We refer to the loop gain of (8.106) as the *compensated* loop gain. Figure 8.23 also shows the magnitude and phase plots of the compensated loop gain, for  $P_{ext0} = 2.5, 0$ , and  $-2.5$  MW. Figure 8.23 illustrates that  $|\ell(j200)| = 1$  for all three operating points. Moreover,  $\angle\ell(j200)$  is  $-89^\circ$ ,  $-112^\circ$ , and  $-135^\circ$ , corresponding to  $P_{ext0} = 2.5, 0$ , and  $-2.5$  MW, respectively. Thus, the closed-loop system is stable for the three operating points with a phase margin ranging from  $45^\circ$  to  $91^\circ$ .

Figure 8.24 illustrates the response of the controlled DC-voltage power port of Figure 8.21 to the start-up process as well as stepwise changes in  $P_{ext}$ . The

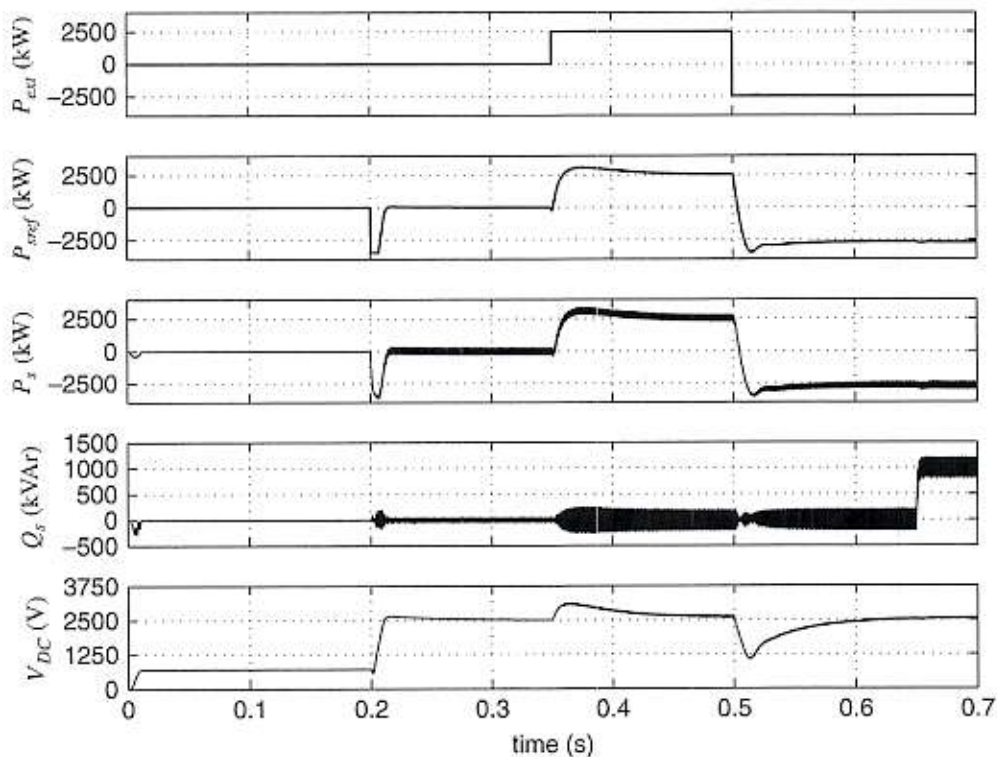


FIGURE 8.24 Dynamic performance of the controlled DC-voltage power port of Example 8.4 when feed-forward compensation is not in service.

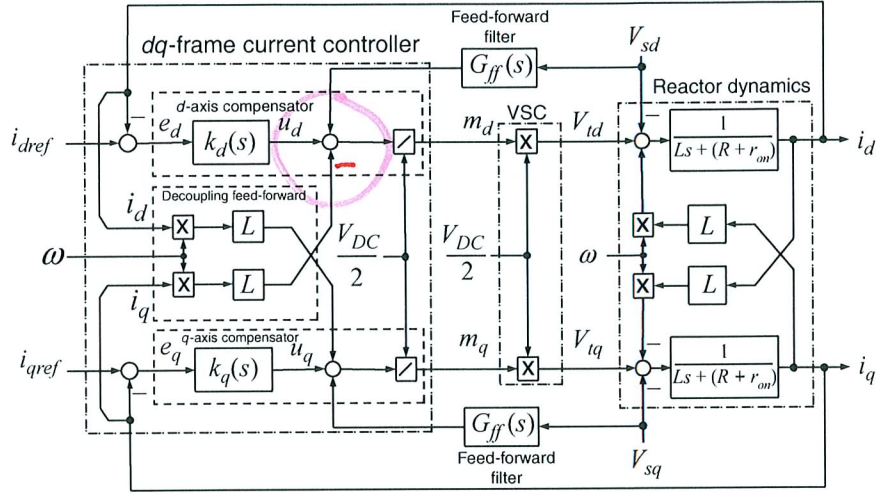


FIGURE 9.2 Control block diagram of a current-controlled VSC system.

where  $\tau_i$  is a design parameter, then  $d$ - and  $q$ -axis closed-loop transfer functions assume the forms

$$I_d(s) = G_i(s)I_{dref}(s) = \frac{1}{\tau_i s + 1} I_{dref}(s), \quad (9.4)$$

$$I_q(s) = G_i(s)I_{qref}(s) = \frac{1}{\tau_i s + 1} I_{qref}(s). \quad (9.5)$$

It is noted that  $\tau_i$  turns out to be the time constant of the first-order, closed-loop, transfer functions. With reference to Figure 9.1, dynamics of the load voltage are described by state-space equations:

$$C_f \frac{dV_{sa}}{dt} = i_a - i_{La}, \quad (9.6)$$

$$C_f \frac{dV_{sb}}{dt} = i_b - i_{Lb}, \quad (9.7)$$

$$C_f \frac{dV_{sc}}{dt} = i_c - i_{Lc}. \quad (9.8)$$

Equations (9.6)–(9.8) constitute the space-phasor equation

$$C_f \frac{d\vec{V}_s}{dt} = \vec{i} - \vec{i}_L. \quad (9.9)$$

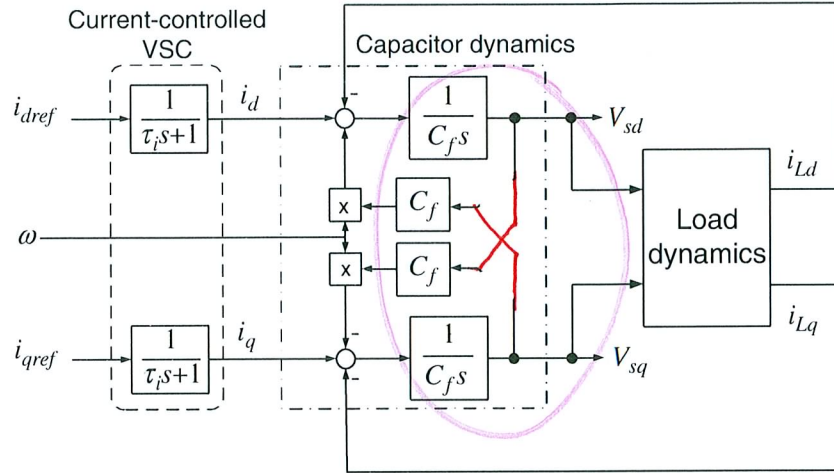


FIGURE 9.3 Block diagram of the load voltage dynamic model.

dynamic order of the load model depend on the load configuration and the number of storage elements<sup>2</sup>.

**EXAMPLE 9.1 Dynamic Model of a Series *RL* Load**

Assume that the load in the system of Figure 9.1 is a three-phase series *RL* branch (Fig. 9.4). With reference to Figure 9.4, we have

$$\begin{aligned}
 L_1 \frac{di_{1a}}{dt} &= -R_1 i_{1a} + V_{sa} - V_{n1}, \\
 L_1 \frac{di_{1b}}{dt} &= -R_1 i_{1b} + V_{sb} - V_{n1}, \\
 L_1 \frac{di_{1c}}{dt} &= -R_1 i_{1c} + V_{sc} - V_{n1},
 \end{aligned}
 \tag{9.16}$$

Equation (9.16) is equivalent to

$$L_1 \frac{d\vec{i}_1}{dt} = -R_1 \vec{i}_1 + \vec{V}_s.
 \tag{9.17}$$

<sup>2</sup>The exception is an ideal, independent, current-sourced load for which  $i_{Ld}$  and  $i_{Lq}$  are independent of  $V_{sd}$ ,  $V_{sq}$ , and  $\omega$ .

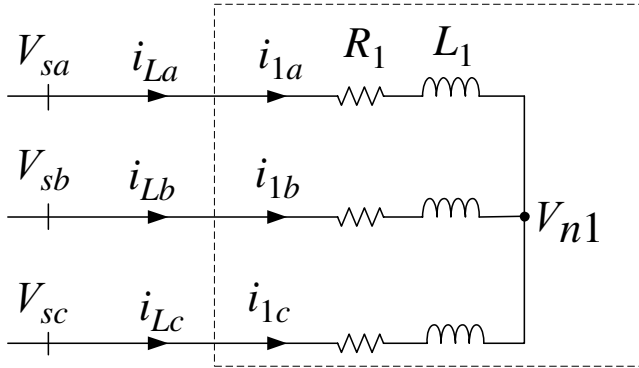


FIGURE 9.4 Series *RL* load of Example 9.1.

Substituting for  $\vec{f} = (f_d + jf_q)e^{j\rho(t)}$  in (9.17) and letting  $d\rho/dt = \omega(t)$ , we obtain

$$\begin{aligned} \frac{di_{1d}}{dt} &= -\frac{R_1}{L_1}i_{1d} + \omega i_{1q} + \frac{1}{L_1}V_{sd} = f_1(i_{1d}, i_{1q}, V_{sd}, V_{sq}), \\ \frac{di_{1q}}{dt} &= -\omega i_{1d} - \frac{R_1}{L_1}i_{1q} + \frac{1}{L_1}V_{sq} = f_2(i_{1d}, i_{1q}, V_{sd}, V_{sq}). \end{aligned} \tag{9.18}$$

In addition,

Replace the highlighted sentence with "It should be noted that if  $w(t)$  is not a constant," (9.19)

Thus, in general, the dynamic system representing the load of Figure 9.4 has two state variables, three inputs, and two outputs. It is interesting to note that even if  $\omega(t)$  is a variable, (9.18) and (9.19) represent a nonlinear dynamic system.

**EXAMPLE 9.2 Dynamic Model of a Composite Load**

Consider the load system of Figure 9.5, which is composed of parallel connection of the load of Figure 9.4 and a series *RLC* branch. The *RLC* branch of the load is described by

$$\begin{aligned} L_2 \frac{di_{2a}}{dt} &= -R_2 i_{2a} + V_{sa} - V_a - V_{n2}, \\ L_2 \frac{di_{2b}}{dt} &= -R_2 i_{2b} + V_{sb} - V_b - V_{n2}, \\ L_2 \frac{di_{2c}}{dt} &= -R_2 i_{2c} + V_{sc} - V_c - V_{n2}, \end{aligned} \tag{9.20}$$

In some applications,  $T_{ext}$  does not depend (or depends weakly) on  $\omega_r$  or  $\theta_r$  and therefore can be regarded as a disturbance input to the control system. However, in most energy conversion applications,  $T_{ext}$  is a function of  $\omega_r$ ,  $\theta_r$ , and other exogenous variables. For example, in a wind turbine  $T_{ext}$  is a nonlinear function of the machine rotor speed, wind speed, and turbine pitch angle. If the pulsating torque of a horizontal-axis wind turbine is also considered, then  $T_{ext}$  is also a nonlinear function of the rotor position,  $\theta_r$ . In general,

$$T_{ext} = f(\omega_r, \theta_r, u_1, \dots, u_n), \quad (10.12)$$

where  $u_1, \dots, u_n$  are exogenous variables. Equations (10.7)–(10.12) describe an electromechanical system consisting of the machine and the mechanical system. Equations (10.7)–(10.9) correspond to the machine electrical dynamics whereas (10.10)–(10.12) describe the mechanical system. The electrical equations can be made decoupled from those of the mechanical system if participation of  $\theta_r$  in (10.7)–(10.9) is compensated. As such, the electromechanical system can be divided into two subsystems: the electrical subsystem for which  $\vec{V}_s$  and  $\vec{V}_r$  are the control inputs and  $T_e$  is the output, and the mechanical subsystem for which  $T_e$  is the control input. Depending on the application,  $\omega_r$ ,  $\theta_r$ , or the mechanical power  $P_m = T_{ext}\omega_r$  can be defined as the output. In this chapter, we concentrate on the control of  $T_e$  by the VSC system.

### 10.3.1 Asynchronous Machine

**10.3.1.1 Machine Model in Rotor-Field Coordinates** In this section, we present the controls for the VSC system of Figure 10.1 that is interfaced with an asynchronous machine. We consider a squirrel-cage asynchronous machine or, equivalently, a wound-rotor asynchronous machine whose rotor terminals are short circuited and rotor current is not measurable. Thus, in (10.7)–(10.9),  $\vec{V}_r = 0$  and  $\vec{i}_r$  is not measurable.

Let us introduce the fictitious space phasor current  $\vec{i}_{mr} = \hat{i}_{mr} e^{j\rho}$  and the change of variable  $(1 + \sigma_r) e^{j\theta_r} \vec{i}_r + \vec{i}_s = \vec{i}_{mr}$ , [43]. Then, we have

$$(1 + \sigma_r) \vec{i}_r + e^{-j\theta_r} \vec{i}_s = \hat{i}_{mr} e^{j(\rho - \theta_r)}. \quad (10.13)$$

Solving for  $\vec{i}_r$  in (10.13), we deduce

$$\vec{i}_r = \frac{\hat{i}_{mr} e^{j\rho} - \vec{i}_s}{1 + \sigma_r} e^{-j\theta_r}. \quad (10.14)$$

it should be noted that  $T_{eref}$  is often either the output of another compensator or the product of an inherent feedback loop. An example of the former is a variable-speed motor drive where  $T_{eref}$  is determined by a speed (or position) control loop that regulates  $\omega_r$  (or  $\theta_r$ ). An example of the latter is a variable-speed wind-power unit where  $T_{eref}$  is set to be proportional to  $\omega_r^2$ . In both cases,  $\omega_r$  is related to  $T_e$  and thus the loop is closed.

The flux regulator and torque controller parts of Figure 10.4 issue the commands  $i_{sdref}$  and  $i_{sqref}$  which, in turn, control  $i_{sd}$  and  $i_{sq}$  based on an inherently, nonlinear, two-input-two-output system. The next subsection shows that by proper control and feed-forward compensation techniques, one can transform the system into two decoupled, single-input-single-output (SISO), linear time-invariant subsystems, each characterized by a first-order transfer function,  $G_i(s)$  (Fig. 10.4); one subsystem relates  $i_{sd}$  to  $i_{sdref}$  whereas the other subsystem relates  $i_{sq}$  to  $i_{sqref}$ . We will also show that by proper selection of parameters of ( $d$ - and  $q$ -axis) compensators, one can make the time constant of  $G_i(s)$  arbitrarily small.

**10.3.1.3 Machine Current Control by VSC System** As discussed in the previous subsection, the machine flux and torque are controlled, respectively, by  $i_{sd}$  and  $i_{sq}$ . However, the VSC can only control the stator voltage.<sup>3</sup> Therefore, one must first develop mathematical expressions to relate  $i_{sd}$  and  $i_{sq}$  to  $V_{sd}$  and  $V_{sq}$ .

The stator terminal voltage and current are related based on (10.1) and (10.3). Substituting for  $\vec{i}_r$  from (10.14) in (10.3), and then for  $\vec{\lambda}_s$  from the resultant in (10.1), we obtain

$$L_m \frac{d}{dt} \left[ \frac{(1 + \sigma_s)(1 + \sigma_r) - 1}{1 + \sigma_r} \vec{i}_s + \frac{1}{1 + \sigma_r} \hat{i}_{mr} e^{j\rho} \right] = \vec{V}_s - R_s \vec{i}_s. \quad (10.23)$$

Defining the machine total leakage factor,  $\sigma$ , as [43]

$$\sigma = 1 - \frac{1}{(1 + \sigma_r)(1 + \sigma_s)}, \quad (10.24)$$

we can rewrite (10.23) as

$$L_m \sigma (1 + \sigma_s) \frac{d \vec{i}_s}{dt} + L_m (1 - \sigma) (1 + \sigma_s) \frac{d}{dt} \left( \hat{i}_{mr} e^{j\rho} \right) = \vec{V}_s - R_s \vec{i}_s. \quad (10.25)$$

Dividing both sides of (10.25) by  $R_s$ , we deduce

$$\sigma \tau_s \frac{d \vec{i}_s}{dt} + (1 - \sigma) \tau_s \frac{d}{dt} \left( \hat{i}_{mr} e^{j\rho} \right) = \frac{1}{R_s} \vec{V}_s - \vec{i}_s, \quad (10.26)$$

<sup>3</sup>The VSC can directly control the stator current if a hysteresis-band current-control strategy is employed rather than the PWM strategy. The main disadvantage of the method is the variable switching frequency.

where  $\tau_s$  is the stator time constant and defined as

$$\tau_s = \frac{L_m(1 + \sigma_s)}{R_s}. \quad (10.27)$$

Substituting for  $\vec{i}_s = (i_{sd} + j i_{sq})e^{j\rho}$  and  $\vec{V}_s = (V_{sd} + j V_{sq})e^{j\rho}$  in (10.26), calculating the derivatives, and multiplying both sides of the resultant by  $e^{-j\rho}$ , we obtain

$$\sigma\tau_s \frac{di_{sdq}}{dt} + i_{sdq} = -j\sigma\tau_s\omega i_{sdq} - j(1 - \sigma)\tau_s\omega \hat{i}_{mr} - (1 - \sigma)\tau_s \frac{d\hat{i}_{mr}}{dt} + \frac{1}{R_s}V_{sdq}, \quad (10.28)$$

where  $\omega = d\rho/dt$  and we have employed  $f_{dq}$  as a compact representation for  $f_d + jf_q$ . Decomposing (10.28) into real and imaginary components, we deduce

$$\left( \sigma\tau_s \frac{di_{sd}}{dt} + i_{sd} \right) = \sigma\tau_s\omega i_{sq} - (1 - \sigma)\tau_s \frac{d\hat{i}_{mr}}{dt} + \frac{1}{R_s}V_{sd}, \quad (10.29)$$

$$\left( \sigma\tau_s \frac{di_{sq}}{dt} + i_{sq} \right) = -\sigma\tau_s\omega i_{sd} - (1 - \sigma)\tau_s\omega \hat{i}_{mr} + \frac{1}{R_s}V_{sq}. \quad (10.30)$$

Equations (10.29) and (10.30) represent a nonlinear system for which  $V_{sd}$  and  $V_{sq}$  are inputs, and  $i_{sd}$  and  $i_{sq}$  are outputs (and also the state variables). Based on (10.29) and (10.30), dynamics of  $i_{sd}$  and  $i_{sq}$  are coupled. Moreover, the system is nonlinear due to the terms  $\omega i_{sd}$ ,  $\omega i_{sq}$ , and  $\omega \hat{i}_{mr}$ , in view of the fact that  $\omega$  and  $\hat{i}_{mr}$  are both functions of  $i_{sd}$  and  $i_{sq}$ . This nonlinearity can be avoided in the control if two new control inputs,  $u_d$  and  $u_q$ , are defined as

$$u_d = \sigma\tau_s\omega i_{sq} - (1 - \sigma)\tau_s \frac{d\hat{i}_{mr}}{dt} + \frac{1}{R_s}V_{sd}, \quad (10.31)$$

$$u_q = -\sigma\tau_s\omega i_{sd} - (1 - \sigma)\tau_s\omega \hat{i}_{mr} + \frac{1}{R_s}V_{sq}. \quad (10.32)$$

Substituting for  $V_{sd}$  and  $V_{sq}$  in (10.29) and (10.30), from (10.31) and (10.32), we obtain

$$\left( \sigma\tau_s \frac{di_{sd}}{dt} + i_{sd} \right) = u_d, \quad (10.33)$$

$$\left( \sigma\tau_s \frac{di_{sq}}{dt} + i_{sq} \right) = u_q. \quad (10.34)$$

Equations (10.33) and (10.34) represent two decoupled first-order subsystems with unity DC gains. The first subsystem controls  $i_{sd}$  by  $u_d$  whereas the second subsystem

Calculating the derivative in (11.11), multiplying both sides by  $e^{j\rho}$ , and decomposing the resultant into real and imaginary components, we obtain

$$V_{sd} = L_g \frac{di_{gd}}{dt} - L_g \omega i_{gq} + \hat{V}_g \cos(\omega_0 t + \theta_0 - \rho), \quad (11.15)$$

$$V_{sq} = L_g \frac{di_{gq}}{dt} + L_g \omega i_{gd} + \hat{V}_g \sin(\omega_0 t + \theta_0 - \rho), \quad (11.16)$$

where  $\omega = d\rho/dt$ . As detailed in Section 8.3.4,  $\omega$  is controlled by the PLL (Fig. 8.5), based on the control law

$$\frac{d\rho}{dt} = \omega(t) = H(p)V_{sq}(t), \quad (11.17)$$

where  $p = d(\cdot)/dt$  is the differentiation operator and  $H(s)$  is the transfer function of the PLL compensator. Thus,  $H(p)f(t)$  ( $f(t)$  is an arbitrary function of time) represents the zero-state response of  $H(s)$  to the input  $f(t)$ . As explained in Section 8.3.4, the PLL compensator includes one integral term and thus  $\omega(t)$  assumes a nonzero steady-state value when  $V_{sq}$  settles at zero. Equations (11.13)–(11.17) represent a dynamic system for which  $V_{sd}$  is the output,  $i_d$  and  $i_q$  are the control inputs, and  $i_{Ld}$  and  $i_{Lq}$  are the disturbance inputs. The system is nonlinear due to the presence of the terms  $\hat{V}_g \cos(\omega_0 t + \theta_0 - \rho)$  and  $\hat{V}_g \sin(\omega_0 t + \theta_0 - \rho)$ . Moreover, the frequency of the VSC system,  $\omega$ , is a dynamic variable that depends on the operating point. To further clarify this point, let us substitute for  $V_{sq}$ , from (11.16), in (11.17):

$$\frac{d\rho}{dt} = L_g H(p) \left( \frac{di_{gq}}{dt} + \omega i_{gd} \right) + \hat{V}_g H(p) \sin(\omega_0 t + \theta_0 - \rho). \quad (11.18)$$

Equation (11.18) indicates that dynamic responses of  $\rho$  and  $\omega$ , in addition to their natural transient components corresponding to  $i_{gd} = i_{gq} = 0$ , include forced components that are functions of  $i_{gd}$  and  $i_{gq}$ . This is in contrast to the case of a stiff grid described by (8.24). Based on (8.24), if the VSC is interfaced with a stiff AC system, the responses of  $\rho$  and  $\omega$  merely include natural transient components; the PLL dynamics are decoupled from those of the rest of the system and the operating point and, therefore, once the PLL reaches the steady state,  $\rho = \omega_0 t + \theta_0$  and  $\omega = \omega_0$ .

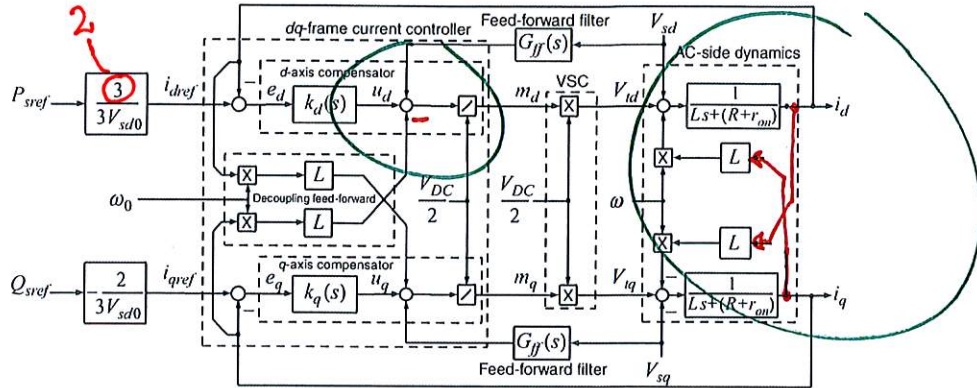


FIGURE 11.5 Control block diagram of the STATCOM  $dq$ -frame current controller (see Section 8.4.1 for details).

approach as the one adopted for the controlled DC-voltage power port (Section 8.6). In contrast, however, in the STATCOM  $Q_s$ , which is usually a free control variable in the controlled DC-voltage power port, is controlled through a closed-loop mechanism that regulates the PCC voltage. The PCC voltage regulation is based on the model of Figure 11.2 or its simplified version (Fig. 11.4). Since  $V_{sq} = 0$ , the control of  $P_s$  and  $Q_s$  is equivalent to the control of  $i_d$  and  $i_q$ , respectively (see equations (4.83) and (4.84)).

The structure of the VSC  $dq$ -frame current controller shown in Figure 8.10, is repeated here as Figure 11.5. There is, however, a minor difference between the control systems of Figures 8.10 and 11.5: if the AC system is stiff, the PLL dynamics are decoupled from those of the other system variables. Thus, once the PLL start-up transients are passed, the angular velocity of the  $dq$ -frame settles to the constant value  $\omega_0$ . This condition holds for the current controller of Figure 8.10, where  $\omega = \omega_0$  appears as a constant parameter in both the plant coupling terms and the controller decoupling terms. However, in the case of the STATCOM,  $\omega$  is a dynamic variable in the plant model, as illustrated in Figure 11.5; this is due to the AC system weakness and the PLL dynamics. Thus, to decouple the plant  $d$ - and  $q$ -axis dynamics, theoretically,  $\omega$  (that is, an output of the PLL) should be used in the controller decoupling terms, rather than  $\omega_0$ . However, accepting a suboptimal (but quite effective) decoupling, we use  $\omega_0$  in the STATCOM current-control scheme, as shown in Figure 11.5.

With reference to Figure 11.5, compensators  $k_d(s)$  and  $k_q(s)$  are

$$k_d(s) = k_q(s) = \frac{k_p s + k_i}{s}. \quad (11.45)$$

fault. As Figure 12.20(a) shows, during the fault  $V_{sabc1}$  is unbalanced. However, due to feed-forward of  $V_{sd1}$  and  $V_{sq1}$  (see Fig. 12.8),  $i_{abc1}$  remains balanced (Fig. 12.20(b)). Moreover, since  $P_{sref1}$  is not changed during the faults period,  $i_{d1}$  remains constant. Therefore, since  $\hat{i}_1 = \sqrt{i_{d1}^2 + i_{q1}^2}$  and  $i_{q1} = 0$ , the amplitude of  $i_{abc1}$  does not change with respect to the prefault condition, as Figure 12.20(b) illustrates. Figure 12.20(c) and (d) shows that  $V_{sabc2}$  and  $i_{abc2}$  are balanced since PCC2 is sound. However, to maintain the balance of (average) real power, the DC-bus voltage controller reduces the absolute value of  $P_{s2-act}$  from 24 to 16 MW (see Fig. 12.19(b)), through the reduction of the amplitude of  $i_{abc2}$  (Fig. 12.20(d)).

Figure 12.21 illustrates the same variables shown in Figure 12.20, but for the case where PCC2 is subjected to the line-to-ground fault. In this case,  $V_{sabc1}$  and  $i_{abc1}$  remain unchanged with respect to the prefault condition, whereas  $V_{sabc2}$  is unbalanced. However, in contrast to the case of the fault at PCC1, the amplitude of  $i_{abc2}$  increases following the fault inception (Fig. 12.21(d)). The reason is that during the fault at PCC2, the DC component of  $P_{s2-act}$  remains equal to the prefault value of  $P_{s2-act}$  as shown in Figure 12.19(b). However, the amplitude of the positive-sequence component of  $V_{sabc2}$  drops due to the imbalance. Consequently, to transfer the same average power as the prefault condition,  $i_{abc2}$  is increased proportionally by the DC-bus voltage controller.

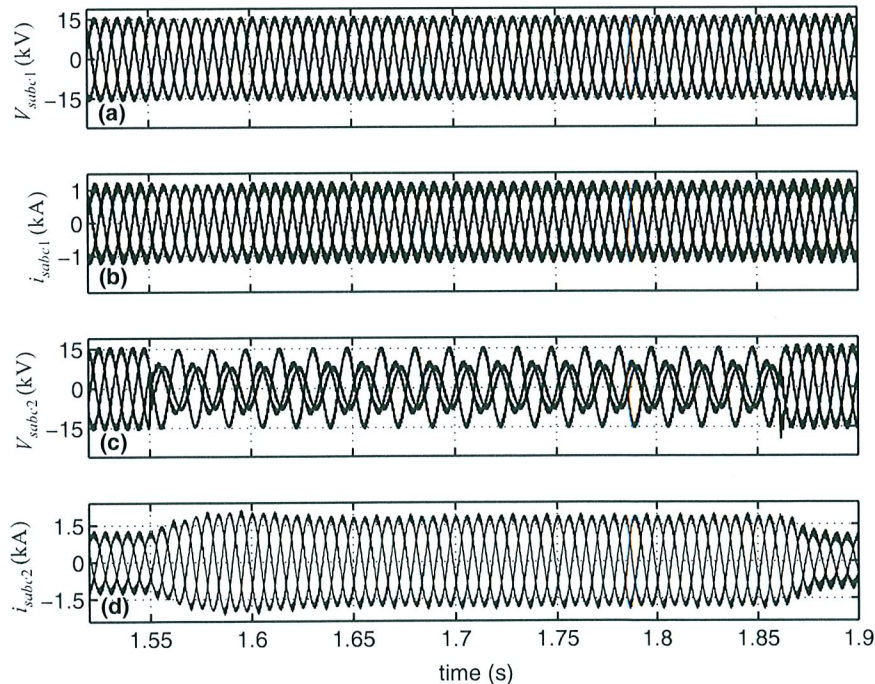


**FIGURE 12.21** Line current and PCC voltage waveforms of the HVDC system of Figure 12.1 when the fault occurs at PCC2.

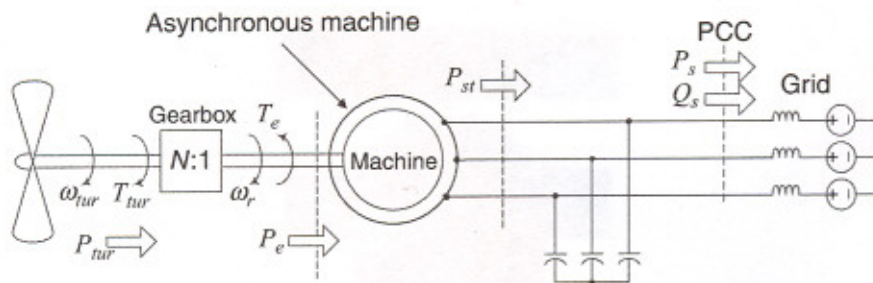


FIGURE 13.1 Schematic diagram of the constant-speed wind-power system.

a few percent

with the utility grid, and thus the machine synchronous frequency is imposed by the grid. The rotor speed of an asynchronous machine is typically within  $\pm 3-8\%$  of the synchronous speed and is thus fairly constant. It should be noted that since the machine operates in the generating mode, its rotor speed is slightly higher than the synchronous speed. An asynchronous machine absorbs reactive power. Therefore, as Figure 13.1 illustrates, the constant-speed wind-power system is equipped with shunt compensation capacitors to maintain the voltage profile and to ensure stable operation, particularly under nonstiff grid conditions.

The constant-speed wind-power system of Figure 13.1 is structurally simple and rugged. However, since the rotor speed is constant, fluctuations in the wind speed and the turbine power are directly transferred to the asynchronous machine and translate into power/voltage fluctuations. This also subjects the drive train and the machine to excessive mechanical and electrical stresses. Moreover, if the grid is not adequately stiff, as in the case of remote wind system installations, the current fluctuations typically cause voltage excursions and flicker [101]. A more noticeable demerit of a constant-speed wind-power system is its relatively poor energy capturing capability and low capacity factor.<sup>3</sup> We will take a closer look at these characteristics in Section 13.3.

### 13.2.2 Variable-Speed Wind-Power Systems

Figures 13.2(a)–(c) illustrate simplified schematic diagrams of three dominant types of variable-speed wind-power systems. Figure 13.2(a) shows the schematic diagram of a variable-speed wind-power system based on the asynchronous machine. The machine frequency and rotor speed are adjusted by a power-electronic converter system that also enables the flow of real power from the variable-frequency machine to the constant-frequency utility grid.

Figure 13.2(b) illustrates a schematic diagram of a variable-speed wind-power system based on the doubly-fed asynchronous machine. In the wind-power system of

<sup>3</sup>The capacity factor of a generator, for example, a wind-power system, is defined as the ratio of its actual delivered energy over a period of time to the energy that could have been delivered over the same period, if the generator had operated at its rated power. Obviously, the capacity factor is also a function of the demand. For a wind-power system, we assume that the rated power is demanded. Typically, a wind-power system has a capacity factor of about 20–40%.

for which the parameter  $\tau$  is 0.066 s. The explanations of the flux observer and its parameters are given in Section 10.3.2. The variable-frequency VSC system also has an embedded  $dq$ -frame current controller (Fig. 10.17) whose compensator  $k(s)$  has the transfer function

$$k(s) = 15.23 \frac{s + 21.86}{s}.$$

For the controlled DC-voltage power port of the wind-power system, that is, Figure 13.11, we have

$$K_V(s) = 299.66 \frac{(s + 19.18)}{s(s + 2083)} \quad [\Omega^{-1}],$$

$$\frac{I_{dref2}(s)}{P_{sref2}(s)} = \frac{2}{3\widehat{V}_{s2}} = 1.361 \quad [(\text{kV})^{-1}],$$

$$\frac{I_{qref2}(s)}{Q_{sref2}(s)} = \frac{-2}{3\widehat{V}_{s2}} = -1.361 \quad [(\text{kV})^{-1}].$$

The commands  $i_{dref2}$  and  $i_{qref2}$  are handed to the  $dq$ -frame current-control scheme of Figure 8.10, which employs the compensators  $k_d(s)$  and  $k_q(s)$ , as

$$k_d(s) = k_q(s) = 0.764 \frac{s + 28.84}{s} \quad [\Omega].$$

Moreover, the transfer function of the feed-forward filters of the current controller is

$$G_{ff}(s) = \frac{1}{8 \times 10^6 s + 1}.$$

$8 \times 10^{-6}$

The transfer function of the compensator  $H(s)$  of the PLL (Fig. 13.10(a)) is

$$H(s) = \frac{142,680(s^2 + 568,516)(s^2 + 166s + 6889)}{s(s^2 + 1508s + 568,516)(s^2 + 964s + 232,324)} \quad [(\text{rad/s})/\text{kV}].$$

Under the nominal grid voltage and with  $i_{rd}$  set to zero, the machine reactive power is  $Q_{s1} = 400$  kVAr, based on (10.116). The filter capacitor  $C_f$  delivers a reactive power of  $Q_f = 49.8$  kVAr. Therefore, to fulfill the operation of the wind-power system at unity power factor, the AC/DC/AC converter system is required to deliver a reactive power of 350.2 kVAr to the grid. Since the variable-frequency VSC system and the controlled DC-voltage power port necessarily handle equal amounts of real power, the reactive power of 350.2 kVAr should

Multiplying both sides of (A.9), (A.10), and (A.11), respectively, by  $(2/3)e^{j0}$ ,  $(2/3)e^{j2\pi/3}$ , and  $(2/3)e^{j4\pi/3}$ , adding the resultants, and employing the definition of the space phasor based on (4.2), we deduce

$$\vec{\lambda}_s = L_s \vec{i}_s + L_m e^{j\theta_r} \vec{i}_r, \quad (\text{A.12})$$

where

$$\begin{aligned} L_s &= L_{ss} - M_{ss}, \\ L_m &= \left(\frac{2}{3}\right) M_{sr}. \end{aligned} \quad (\text{A.13})$$

### A.3.3 Rotor Flux Space Phasor

Similarly, the flux linked by the rotor windings can be formulated as

$$\begin{aligned} \lambda_{ra} &= L_{rr}i_{ra} + M_{rr}i_{rb} + M_{rr}i_{rc} \\ &+ M_{sr} \cos(\theta_r) i_{sa} + M_{sr} \cos\left(\theta_r - \frac{2\pi}{3}\right) i_{sb} + M_{sr} \cos\left(\theta_r + \frac{2\pi}{3}\right) i_{sc}, \end{aligned} \quad (\text{A.14})$$

$$\begin{aligned} \lambda_{rb} &= M_{rr}i_{ra} + L_{rr}i_{rb} + M_{rr}i_{rc} \\ &+ M_{sr} \cos\left(\theta_r + \frac{2\pi}{3}\right) i_{sa} + M_{sr} \cos(\theta_r) i_{sb} + M_{sr} \cos\left(\theta_r - \frac{2\pi}{3}\right) i_{sc}, \end{aligned} \quad (\text{A.15})$$

$$\begin{aligned} \lambda_{sc} &= M_{rr}i_{ra} + M_{rr}i_{rb} + L_{rr}i_{rc} \\ &+ M_{sr} \cos\left(\theta_r - \frac{2\pi}{3}\right) i_{sa} + M_{sr} \cos\left(\theta_r + \frac{2\pi}{3}\right) i_{sb} + M_{sr} \cos(\theta_r) i_{sc}, \end{aligned} \quad (\text{A.16})$$

where  $L_{rr}$  and  $M_{rr}$  are the self- and mutual inductances, respectively. Due to the symmetry of the magnetic structure,  $L_{rr}$  and  $M_{rr}$  are constant parameters. However, the mutual inductance between a rotor winding and a stator winding is a function of the rotor angle  $\theta_r$ , as discussed in Section A.3.2. Multiplying both sides of (A.14), (A.15), and (A.16), respectively, by  $(2/3)e^{j0}$ ,  $(2/3)e^{j2\pi/3}$ , and  $(2/3)e^{j4\pi/3}$ , adding the resultants, and employing the definition of the space phasor based on (4.2), we deduce

$$\vec{\lambda}_r = L_r \vec{i}_r + L_m e^{-j\theta_r} \vec{i}_s, \quad (\text{A.17})$$

where

$$L_r = L_{rr} - M_{rr}, \quad (\text{A.18})$$

and  $L_m$  is defined by (A.13).

$$T_e = \left( \frac{3}{2} L_m \right) \text{Im} \left\{ \vec{i}_s \vec{i}_r'^* \right\}, \quad (\text{A.25})$$

where  $\omega_r = d\theta_r/dt$  is the rotor angular velocity. The term  $j\omega_r \vec{\lambda}'_r$  in (A.22) represents a voltage component, proportional to the rotor speed, which can be regarded as the rotor back EMF.

Let us define the rotor and stator leakage factors as

$$\sigma_s = \frac{L_s}{L_m} - 1, \quad (\text{A.26})$$

$$\sigma_r = \frac{L_r}{L_m} - 1. \quad (\text{A.27})$$

Then, (A.23) and (A.24) can be rewritten as

$$\vec{\lambda}_s = \sigma_s L_m \vec{i}_s + L_m \underbrace{(\vec{i}'_r + \vec{i}_s)}_{\vec{i}_m}, \quad (\text{A.28})$$

$$\vec{\lambda}'_r = \sigma_r L_m \vec{i}'_r + L_m \underbrace{(\vec{i}'_r + \vec{i}_s)}_{\vec{i}_m}, \quad (\text{A.29})$$

Based on (A.3), (A.22), (A.28), and (A.29), Figure A.2 presents an equivalent circuit for the machine. The equivalent circuit of Figure A.2 is known as the *air-gap flux model* or the *T-form model* of the machine [109]. The equivalent circuit of Figure A.2 represents the squirrel-cage asynchronous machine, if  $\vec{V}'_r$  is zero. In the doubly-fed asynchronous machine, in addition to  $\vec{V}_s$ , the rotor voltage vector  $\vec{V}'_r$  is also controllable. The equivalent circuit of Figure A.2 is valid for both dynamic and steady-state conditions.

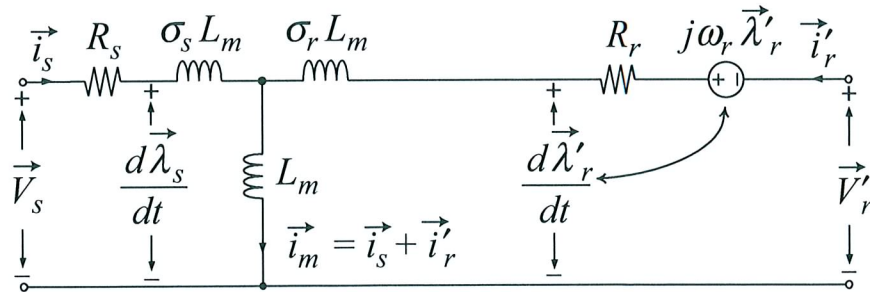


FIGURE A.2 Space-phasor domain equivalent circuit of the symmetrical three-phase machine.